POLITECNICO DI TORINO

Scuola di Dottorato

Dottorato di Ricerca in Fisica
Dipartimento Scienza Applicata e Tecnologia
Coordinatore del Dottorato: Prof.ssa Arianna Montorsi

Ciclo XXV

Tesi di Dottorato

Quantum Characterization of Single Photon Detectors

Relatori:

Dr. Giorgio Brida

Prof. Vittorio Penna

Maria Griselda Mingolla

Febbraio 2014

To Ana and Juan

Abstract

The research activities described in this thesis have basically an experimental profile, and were realized in the Quantum Optics Laboratories of the Optic Division in the Istituto Nazionale di Ricerca Metrologica (I.N.Ri.M.).

The experiments presented here are oriented to the characterization of single- and few-photon detectors calibration, exploiting quantum properties.

The first chapter has an introductory character, oriented to the study of nonlinear optics phenomena and focused in the spontaneous parametric down conversion (PDC) process. After the quantization of the free electromagnetic field, we recall the quantum theory of PDC.

In the second chapter the Klyshko's two-photon calibration technique is presented and applied to an Avalanche Photo Diode (APD) based single photon counting module.

Chapter three is an introduction to quantum measurements and quantum operation theories where the concept of positive-operator valued measurement (POVM) is presented.

In chapter four, the quantum characterization of a true photon-number resolving detector (PNRD) based on a transition edge sensor (TES) is presented. In this experiment, the POVM of the TES is reconstructed by realizing a tomography of the detection process's quantum operation, using as a probe a set of known coherent states.

In the fifth and last chapter, the POVM of a tree type PNRD is reconstructed

exploiting strong quantum correlations of PDC twin beams.

This thesis is mainly based on the following papers:

- G. Brida, L. Ciavarella, I. P. Degiovanni, M. Genovese, A. Migdall, M. G. Mingolla, M. G. A. Paris, F. Piacentini and S. V. Polyakov, "Ancilla-Assisted Calibration of a Measuring Apparatus", *Phys. Rev. Lett.* 108, 253601 (2012).

- Giorgio Brida, Luigi Ciavarella, Ivo P. Degiovanni, Marco Genovese, Lapo Lolli, Maria G. Mingolla, Fabrizio Piacentini, Mauro Rajteri, Emanuele Taralli, Matteo G. A. Paris, "Quantum characterization of superconducting photon counters", *New J. Phys.* 14, 085001 (2012).

- M. G. Mingolla, F. Piacentini, A. Avella, M. Gramegna, L. Lolli, A. Meda, I. Ruo Berchera, E. Taralli, P. Traina, M. Rajteri, G. Brida, I. P. Degiovanni, M. Genovese, " Quantum and classical characterization of single/few photon detectors". arXiv:1103.2991v4. Quantum Matter in press.

Contents

Introduction

In the last decades, quantum optics experiments based on intensity light measurements have been realized mainly with intense (macroscopic) fields or at single-photon level, while photon counting with few-photon light (up to 100 photons) is a rather unexplored measurement regime. Despite this fact there are several applications that may benefit from the transition from single-photon to few photon measurement regime, such as e.g. bioluminescence detection [1], single molecule spectroscopy [2], fluorescence life time measurements [3, 4], medical applications using optical tomography [5], investigation on quantum optics foundations [6], quantum communication [7–9], computation [10,11] and metrology [12, 13].

Although single-photon detectors and, most recently, few-photon detectors, are rather diffused, a huge development in single photon technologies [14] is mandatory, as well as a proper metrological framework ensuring their standardization, to bring quantum applications in citizens life.

In this frame, quantum radiometry (a quite new branch of radiometry) is growing within the metrology community not only to be ready to provide high level technological solutions to the actual and future problems faced in the fields of applications, but also to improve their own methodologies, carrying out an innovative approach to optical radiation measurements in terms of number of photons [15–17].

In particular, quantum radiometry concerns the absolute measurement of photon quantities based on fundamental physical phenomena, and refers to the quantum theory of light by definition of a single quantum of radiation as a photon: at very low radiant

powers, radiant or luminous quantities can be replaced usefully by quantities related to the number of photons. In fact when the light level approaches picowatt and femtowatt (10^4 - 10^7 photons/s) photon counting techniques are employed.

We underline that one of the biggest challenge of the European Metrology Research Programme (EMRP) is the redefinition of the SI base unit of luminous intensity, the candela, in terms of photon number, the so-called quantum candela, expressed by the qu-Candela project under the IMERA programme [18]. The qu-Candela project forms the backbone of the EMRP roadmap "Towards quantum photon-based standards for optical radiation", and identifies for its realization some fundamental steps, as obtaining an absolute technique for the measurement of quantum efficiency of single-photon detectors, and producing reliable sources of single photons with predictable parameters, both at visible and telecommunication wavelengths.

An ideal single-photon detector is considerer to be one for which: the detection efficiency (the probability that a photon incident upon the detector is successfully detected) is 100%, the dark-count rate (rate of detector output pulses in the absence of any incident photons) is zero, the dead time (time after a photon-detection event during which the detector is incapable of detecting a photon) is zero, and the timing jitter (variation from event to event in the delay between the input of the optical signal and the output of the electrical signal) is zero. Additionally, an ideal single-photon detector would have the ability to distinguish the number of photons in an incident pulse (referred to as "photon-number resolution" (PNR)); many single-photon detectors (e.g., single-photon avalanche photodiodes, photomultiplier tubes, superconducting nanowire single-photon detectors) typically used are not photon-number resolving and can only distinguish between zero photons and more than zero photons. Deviations from these ideals negatively impact experiments in varying ways depending on the detector characteristic and measurement involved [19].

Almost all single-photon detectors involve the conversion of a photon into an electrical signal of some sort. It is the job of the detector electronics to ensure that each photo-generated electrical signal is detected with high efficiency. Additional electronics is often

required after detection to return the detector as quickly as possible back to a state that allows it to detect another photon. The electronics is often as important as the detector itself in achieving the ideal characteristics outlined above.

The most commonly used single-photon detectors are non-photon-number-resolving detectors. While detecting a single photon is a difficult task, discriminating the number of incident photons is even more difficult. Because the energy of a single photon is so small ($\approx 10^{-19}J$), its detection requires very high gain and low noise. In many detectors this is achieved by converting the incoming photon into a charge carrier and then using a high voltage avalanche process to convert that single charge into a macroscopic current pulse. In particular, the single photon avalanche detectors (SPADs) are typically run in what is referred to as "Geiger-mode", where a bias voltage greater than the diode's breakdown voltage is applied. Thus when a charge is generated by an incoming photon, the charge multiplication (or avalanche) proceeds until it saturates at a current typically limited by an external circuit. The saturated avalanche current must be stopped by lowering the bias voltage below the breakdown voltage before the SPAD can respond to a subsequent incoming optical pulse. As a result, the SPAD dead time range from tens of nanoseconds to 10 μs.

Concerning PNR detectors it is important to discuss what "photon-number-resolution" means, and to lay out the degrees of photon-number-resolution that a detector can have. First let highlight that detectors classified as photon-number-resolving do not tell the true number of incident photons unless their efficiency is 100%, the measured number is at best just a lower estimate, and in the presence of dark counts it is not even that. In addition we attempt to categorize the degree of PNR capability into three groups defined as (a) "no PNR capability" for devices that are typically operated as a photon or no-photon device (for example SPAD), (b) "some PNR capability" for devices made of multiple detectors that individually have no PNR capability and thus are limited in the maximum photon number that can be resolved to the number of individual detectors, and (c) "full PNR capability" for devices whose output is inherently proportional to the number of photons, even if their detection efficiency is low and their proportional

response ultimately saturates at high input photons levels. As an example, we consider a PNR detector based on a superconducting transition edge sensor (TES). This detector operates as a bolometer: that is electromagnetic radiation is absorbed and, via the heating of a material with a temperature-dependent electrical resistance, the energy of incident radiation is obtained. To achieve the extreme sensitivity required to detect the energy of a single photon, the heat capacity of the absorber must be made extremely small and the thermal sensor must exhibit a large response to a small temperature change. As a thermal device which measures energy absorbed, its output is proportional to the number of photons absorbed, thus it can provide photon-number resolution. The extreme temperature sensitivity is achieved by constructing the thermal sensor from a thin layer of superconducting material (deposited on an insulating substrate) made to operate at a temperature in its transition between superconducting and normal resistance, so a slight change in temperature yields a large change in resistance.

This thesis is focused in study the behaviour of three kinds of single-photon detectors. With this aim different experiments where performed in the Optic Laboratory of the Istituto Nazionale di Ricerca Metrologica (INRIM) at Turin, Italy. The research work of this thesis is based in this three experiments, presenting in each particular case, a different approach to the detector characterization.

In the following we present our research activity.

We begin the thesis with an introduction of the nonlinear optics phenomena focused in the spontaneous parametric down conversion (PDC) process. In a first approach, the phenomena is analysed classically and, in the last section of the chapter, quantum theory of radiation is introduced and PDC process is analysed in therms of the interaction of quantized fields.

In the second chapter of this thesis an experiment focused on the detection quantum efficiency, η, defined as the overall probability of observing the presence of a single photon impinging on the detector is presented. An absolute measurement technique (named Klyshko two-photon technique) based on correlated photons obtained from parametric

down conversion, is applied to calibrate a single-photon avalanche detector.

The third chapter introduces the theories of quantum measurements and quantum operation as well as the concept of positive operator values measure (POVM).

In the fourth chapter we address the quantum characterization of a photon counter based on a TES. Here the detection process is considered as a quantum operation, thus the technique consists in realizing the tomography of the quantum operation using as a probe a known set of coherent states of different amplitudes. This experiment is the first experimental tomography of the POVM of a TES.

In the last chapter of this thesis, the first experimental POVM reconstruction that takes explicit advantage of a quantum resource, i.e. nonclassical correlations with an ancillary state, is presented. A POVM of a tree type photon-number-resolving detector is reconstructed by using strong quantum correlations of twin beams generated by parametric down-conversion. Our reconstruction method is more statistically robust than POVM reconstruction methods that use classical input states.

This thesis work gave way to two publications, that are presented at the end of this thesis. A third paper is submitted to a Quantum Matter journal and is under evaluation at the moment of this thesis presentation. This article is although included at the end of the thesis.

Chapter 1

Nonlinear optics and photon source generation

The propagation of electromagnetic waves through nonlinear media gives rise to "vibrations" at harmonics of the fundamental frequency, at sum and difference frequencies, and so on. Similar effects are observed in the optical frequency range when light waves propagates through a weakly non linear optical dielectric (for example, a nonlinear crystal).

The wavelength range of a laser source passing through a non linear optical dielectric can be considerably increased: the radiation frequency ω_0 of the laser may be both transformed to high harmonics of the original frequency ($2\omega_0$, $3\omega_0$, etc.) [20], or can cause a simultaneous generation of radiations ω_1 and ω_2 where $\omega_0 = \omega_1 + \omega_2$. In the latter effect, known as parametric down conversion (PDC) process, one photon of the laser beam is converted into two new, strongly correlated in time of emission and wavelength due to constraints of energy and momenta conservation.

1.1 Nonlinear optics

The discover of the second harmonic generation effect in 1961 by Franken *et al.* [21] is often referred as the birth of nonlinear optics. Since its beginning, interest in the field

of nonlinear optics has grown continuously, with an increasing research over a wide type of materials presenting this phenomena [22–25]. Nowadays, the interest in non linear optics ranges from fundamental studies of the interaction of light with matter [26,27], to several applications such as implementation of quantum information protocols [28, 29], quantum metrology techniques [16, 30], etc.

In nonlinear optical effects, the response of a material system to an applied optical field depends in a nonlinear way on the strength of the optical field. Conversion of a light-wave frequency (multiplication, division, mixing) is possible in nonlinear optical crystals for which the refractive index n is a function of the electric field strength vector $\mathbf{E}$ of the light wave

$$n(\mathbf{E}) = n_0 + n_1(\mathbf{E}) + n_2\mathbf{E}^2 + ... \tag{1.1}$$

where n_0 is the refractive index in the absence of the electric field, and n_1, n_2 and so on are the coefficients of the series expansion of $n(\mathbf{E})$.

To be more specific about nonlinearity definition, let us consider how the dielectric polarization vector $\mathbf{P}$ of a material (dipole moment of unite volume of the media) depends on the strength $\mathbf{E}$ of an applied optical field. In the case of linear optics the induced dielectric polarization goes linearly with the electric field strength obeying the equation [31]

$$\mathbf{P}(\mathbf{E}) = \chi^{(1)}\mathbf{E} \tag{1.2}$$

where the constant of proportionality $\chi^{(1)}$ is the linear dielectric susceptibility. In nonlinear optics, the optical response can be described by generalizing Eq. (1.2) by expressing the dielectric polarization $\mathbf{P}$ as a power series in $\mathbf{E}$

$$\begin{aligned} \mathbf{P}(\mathbf{E}) &= \chi^{(1)}\mathbf{E} + \chi^{(2)}\mathbf{E}\mathbf{E} + \chi^{(3)}\mathbf{E}\mathbf{E}\mathbf{E} + ... \\ &\equiv \mathbf{P}^{(1)} + \mathbf{P}^{(2)} + \mathbf{P}^{(3)} + ... \end{aligned} \tag{1.3}$$

the quantities $\chi^{(2)}$, $\chi^{(3)}$ and so on are known as the non linear suceptibility coefficients

(square, cubic and so on, respectively) [32]. $\mathbf{P}^{(2)}$ and $\mathbf{P}^{(3)}$ are known as the second and the third-order nonlinear polarization, respectively. The following equations hold

$$\begin{aligned} \chi^{(1)} &= \tfrac{1}{4\pi}(\epsilon_0 - 1) = \tfrac{1}{4\pi}(n_0^2 - 1); \\ \chi^{(2)} &\cong \tfrac{1}{2\pi} n_0 n_1;\ \chi^{(3)} \cong \tfrac{1}{2\pi} n_0 n_2; \end{aligned} \tag{1.4}$$

where ϵ_0 is the dielectric constant in absence of the electric field. In the general case of anisotropic crystals, the quantities ϵ_0, n, and χ are tensors of the corresponding ranks. Physical processes that occur as a result of the second-order dielectric polarization $\mathbf{P}^{(2)}$ tend to be distinct from those that occur as a result of the third-order dielectric polarization $\mathbf{P}^{(3)}$. Second-order nonlinear optical interactions can occur only in noncentrosymmetric crystals, that is, in crystals that do not have inversion symmetry. Since liquids, gases, and many crystals exhibit inversion symmetry, $\chi^{(2)}$ vanishes for such media, and consequently in such materials second-order nonlinear optical interactions are not produced. On the other hand, third-order nonlinear optical interactions (i.e., those described by a $\chi^{(3)}$ susceptibility) can occur for both centrosymmetric and noncentrosymmetric media [31].

In general, the nonlinear susceptibilities have a rather small magnitude. This means that when the electric field amplitude is small, the non linear terms are negligible and we have a linear relation between $\mathbf{P}$ and $\mathbf{E}$ as it is assumed in linear optics. When the electric field is large, the non linear terms in Eq. (1.3) cannot be neglected and we enter in the domain of nonlinear optics. This thesis will be restricted to the study of three fields interactions occurring in crystals with square nonlinearity ($\chi^{(2)} \neq 0$).

For anisotropic media the coefficients $\chi^{(1)}$, $\chi^{(2)}$ in Eq. (1.3) are, in the general case, tensors of the second and third ranks, respectively. For uniaxial crystals in crystallophysical coordinates X, Y, Z, where Z is the optic axis, the tensor $\chi^{(1)}$ is diagonal [20].

In practice the tensor d_{ijk} is used instead of the second-order susceptibility tensor $\chi^{(2)}_{ijk}$, being both interrelated by the equation

$$\chi^{(2)}_{ijk} = 2d_{ijk} \tag{1.5}$$

where the indices ijk refer to the Cartesian components of the fields.

The expression (1.3) can be rewritten in a reduced form (with respect to the components):

$$P_i = \chi_{ij}^{(1)} E_j + 2 d_{ijr} E_j E_r + ... \tag{1.6}$$

where the summation on repeated indices is understood.

Since any linearly polarized wave in a uniaxial crystal can be represented as a superposition of two waves with "ordinary" and "extraordinary" polarizations, we provide the components of a unit vector $\mathbf{p}$ given in polar coordinates θ and φ along the crystallophysical axis X, Y, Z where Z is the optic axis and $|\mathbf{p}| = 1$:

$$\begin{aligned} \mathbf{p}^o &= (-sin\varphi, cos\varphi, 0), \\ \mathbf{p}^e &= (cos\theta cos\varphi, cos\theta sin\varphi, -sin\theta). \end{aligned} \tag{1.7}$$

The equations for calculating the conversion efficiency use the effective nonlinearity coefficients, which comprise all summation operations along the polarization directions of the interacting waves:

$$d_{eff} = d\mathbf{p}_p\mathbf{p}_s\mathbf{p}_i = d\mathbf{p}_s\mathbf{p}_p\mathbf{p}_i = d\mathbf{p}_i\mathbf{p}_s\mathbf{p}_p. \tag{1.8}$$

Depending on the type of interaction, the vector components $\mathbf{p}$ are calculated by Eq. (1.7), and the product (1.8) is found by the known rules of vector algebra. The calculation of d_{eff} for biaxial crystals by the above procedure is valid only when radiation propagates in the principal planes.

1.2 Second-order nonlinear phenomena

The second order nonlinear polarization is given by the second term of Eq. (1.3). If the medium is excited by cosinusoidal waves with angular frequencies ω_1 and ω_2 and with amplitudes $\mathcal{E}_1$ and $\mathcal{E}_2$ respectively, then the nonlinear polarization will be

$$\begin{aligned} \mathbf{P}^{(2)} &= \chi^{(2)} \times \mathcal{E}_{\mathbf{1}} cos(\omega_1 t) \times \mathcal{E}_{\mathbf{2}} cos(\omega_2 t) \\ &= \chi^{(2)} \mathcal{E}_{\mathbf{1}} \mathcal{E}_{\mathbf{2}} \tfrac{1}{2} [cos(\omega_1 t + \omega_2 t) cos(\omega_1 t - \omega_2 t)] \end{aligned} \tag{1.9}$$

from Eq. (1.9) we can see that the second order nonlinear response generates an oscillating polarization at the sum and difference frequencies of the input fields, $\omega_{sum} = (\omega_1 + \omega_2)$ and $\omega_{diff} = (\omega_1 - \omega_2)$. The generation of these new frequencies by non linear optical processes are known as sum frequency mixing and difference frequency mixing. In the particular case that $\omega_1 = \omega_2 = \omega$, then $\omega_{sum} = 2\omega$ and the effect is called frequency doubling or second harmonic generation.

The non linear process can also work backward, splitting a beam of frequency ω into two beams of frequency ω_1 and ω_2, where $\omega = \omega_1 + \omega_2$, this process is the known PDC process [33]. Because the experiments involved in this thesis exploits the latter process, we will focus our study in it.

1.3 Spontaneous parametric down conversion process

Spontaneous parametric down conversion process, also known as parametric fluorescence, is a process in which a photon of frequency ω_p interacts with a nonlinear crystal with $\chi^{(2)} \neq 0$ and spontaneously decay in two correlated photons (twin photons) with lower energy. This two new photons are known as signal (s) and idler (i) for historical reasons, and have frequencies ω_s and ω_i respectively [34]. The three interacting fields obeys the energy and momentum conservation law (phase matching conditions):

$$\begin{aligned} \omega_p &= \omega_s + \omega_i \\ \mathbf{k}_p &= \mathbf{k}_s + \mathbf{k}_i \end{aligned} \tag{1.10}$$

where $\mathbf{k}_j$ are the wave vectors corresponding to the waves with frequencies ω_j $(j = p, s, i)$

$$|\mathbf{k}_j| = k_j = \frac{\omega_j n(\omega_j)}{c} = \frac{\omega_j}{v(\omega_j)} = \frac{2\pi n_j}{\lambda_j} = 2\pi n_j \nu_j \tag{1.11}$$

where the quantities $v(\omega_j)$, $n_j = n(\omega_j)$, λ_j and ν_j are the phase velocity, refractive index, wavelength, and wave number at frequency ω_j respectively. The relative location of wave vectors under phase matching conditions can be either collinear (scalar phase matching), with the down-converted photons emitted along the same path in the central wave mode direction, or non-collinear (vector phase matching), when there is an angle between the two emitted photons directions (Figure 1.1). The phase matching conditions are fulfilled only in anisotropic crystals with interaction of differently polarized waves. In addition, PDC can be degenerate, where the down-converted photons have the same frequency, while if their frequencies are different we call such configuration as non-degenerate [20].

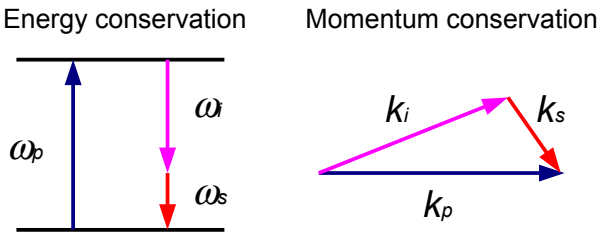

Figure 1.1: Phase matching conditions for a generic non collinear and non degenerate case of PDC process.

In uniaxial crystals a special direction exists called the optical axis (Z axis). The plane containing the Z axis and the wave vector **k** of the pump light waves is named principal plane. The light beam whose polarization (i.e., direction of the vector E oscillations) is normal to the principal plane is called ordinary beam (or *o*-beam). The beam polarized in the principal plane is known as extraordinary beam or *e*-beam [34,35]. The refractive index of the *o*-beam does not depend on the propagation direction, whereas for the *e*-beam it does.

The difference between the refractive indices of the ordinary and extraordinary beams is known as birefringence Δn. The value of Δn is zero along the optic axis Z and maximum in the direction normal to this axis. The refractive indices of the ordinary and extraordinary beams in the plane normal to the Z axis are termed the principal values and are denoted by n_o and n_e, respectively. The refractive index of the extraordinary

waves is, in general, a function of the polar angle θ between the Z axis and the vector $\mathbf{k}$, and it is determined by the equation

$$n_e(\theta) = n_o \sqrt{\frac{1 + tan^2\theta}{1 + (n_o/n_e)^2 tan\theta}}. \tag{1.12}$$

If $n_o > n_e$, the crystal is negative; if $n_o < n_e$, it is positive. The graph of the refractive indices is a sphere with radius n_o for an ordinary beam and an ellipsoid of rotation with semi-axis n_o and n_e for an extraordinary beam (the axis of the ellipsoid of rotation is the Z axis). In the Z-axis direction the sphere and ellipsoid are in contact with each other. In a negative crystal the ellipsoid is inscribed in the sphere, whereas in a positive crystal the sphere is inscribed in the ellipsoid [20].

When a plane light wave propagates in uniaxial crystal, the direction of propagation of the wave phase (vector $\mathbf{k}$) generally does not coincide with that of the wave energy. The direction of wave energy can be defined as the normal to the tangent drawn at the point of intersection of vector $\mathbf{k}$ with the $n(\theta)$ curve. For an ordinary wave the $n(\theta)$ dependence is a sphere with radius n_o. Therefore, the normal to the tangent coincides with the wave vector $\mathbf{k}$. For an extraordinary wave the normal to the tangent (with the exception of the case $\theta = 0°$ and $\theta = 90°$) does not coincide with the wave vector $\mathbf{k}$ but is rotated from it by the birefringence angle

$$\rho(\theta) = \pm arctan[(n_o/n_e)^2 tan\theta] \mp \theta \tag{1.13}$$

where the upper signs refer to a negative crystal and the lower signs to a positive one.

The correlation between ρ and θ may serve as the basis for a simple way to orient uniaxial single crystal. Let a laser beam with an arbitrary linear polarization fall on the input face of a crystal of thickness L. After passing through the crystal, the beam is divided into two orthogonally polarized beams that, at the output face of the crystal, are separated by

$$\delta = L\ tan\rho \tag{1.14}$$

To fulfil the phase-matching condition in three-frequency interaction, differently polarized waves should be considered. The phase-matching configurations, are usually classified by type, if the signal and idler beams have identical polarizations is referred to as type-I phase-matching, while in type-II phasematching the signal and idler polarizations are orthogonal. In parametric down conversion, for the case of type-I phase matching in negative crystals,

$$\mathbf{k_p^e} = \mathbf{k_s^o} + \mathbf{k_i^o} \tag{1.15}$$

(this is called *ooe* phase matching). In the positive crystals

$$\mathbf{k_p^o} = \mathbf{k_s^e} + \mathbf{k_i^e} \tag{1.16}$$

(*eeo* phase matching).

In the case of type-II phase matching in negative crystals, the pump field is an extraordinary wave and signal and idler have different polarizations

$$\begin{aligned} \mathbf{k}_p^e &= \mathbf{k}_s^o + \mathbf{k}_i^e \\ \mathbf{k}_p^e &= \mathbf{k}_s^e + \mathbf{k}_i^o \end{aligned} \tag{1.17}$$

(*oee* and *eoe* phase matching respectively) while in positive crystals is an ordinary wave

$$\begin{aligned} \mathbf{k}_p^o &= \mathbf{k}_s^o + \mathbf{k}_i^e \\ \mathbf{k}_p^o &= \mathbf{k}_s^e + \mathbf{k}_i^o \end{aligned} \tag{1.18}$$

(*oeo* and *eoo* phase matching respectively).

The photon pairs generated by parametric down conversion are strongly correlated in time and space due to the conservation rules, Eq. (1.10). The energy and momentum conservation between the pump and the down-converted photons generates a correlation between the emission direction and the frequencies of the two "daughter" photons, although the momentum and the frequency of each photon is undetermined. The net result is that the down-converted photons typically exit the crystal collinearly or at small

angles with respect to the pump beam, and photons of the same pair propagate along two different directions of emission, (Figure 1.2). Because various geometries satisfy the phase-matching constraints, a broad spectrum of down-converted light can be obtained, i.e. the wavelengths of the down-converted photons can range from the wavelength of the incoming one to the limit of crystal transparency.

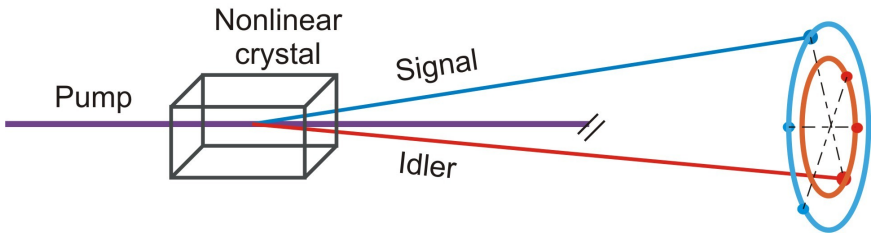

Figure 1.2: Spontaneous parametric down conversion process.

1.4 Quantum theory of radiation

With the goal of quantizing the electromagnetic field in free space, it is convenient to begin with the classical description of the field based on Maxwell's equations. In vacuum, with no charge or current, these equations relate the vectors of electric field $\mathbf{E}$ and magnetic field $\mathbf{H}$, together with the displacement vector $\mathbf{D}$ and inductive vector $\mathbf{B}$, as follow:

$$\nabla \times \mathbf{H} = \frac{\partial \mathbf{D}}{\partial t} \tag{1.19}$$

$$\nabla \times \mathbf{E} = -\frac{\partial \mathbf{B}}{\partial t} \tag{1.20}$$

$$\nabla \cdot \mathbf{B} = 0 \tag{1.21}$$

$$\nabla \cdot \mathbf{D} = 0 \tag{1.22}$$

with the constitutive relations

$$\mathbf{B} = \mu_0 \mathbf{H} \tag{1.23}$$

$$\mathbf{D} = \varepsilon_0 \mathbf{E}. \tag{1.24}$$

Here μ_0 is the magnetic permeability of free space and ε_0 is the electric permittivity of free space, and $\mu_0 \varepsilon_0 = c^{-2}$ with c the speed of light in vacuum.

It follows, on taking the curl of Eq. (1.20) and using Eqs. (1.19),(1.22), (1.23), (1.24) and the relation $\nabla \times (\nabla \times \mathbf{E}) = \nabla(\nabla \cdot \mathbf{E}) - \nabla^2 \mathbf{E}$, that $\mathbf{E}(\mathbf{r}, t)$ satisfies the wave equation

$$\nabla^2 \mathbf{E} - \frac{1}{c^2} \frac{\partial^2 \mathbf{E}}{\partial t^2} = 0. \tag{1.25}$$

We first consider the electric field with a spatial dependence suited for a cavity resonator of length L. We take the electric field to be linearly polarized in the x-direction and expand in the normal modes of the cavity

$$E_x(z, t) = \sum_j A_j q_j(t) \sin(k_j z) \tag{1.26}$$

where q_j is the normal mode amplitude with length dimension, $k_j = j\pi/L$, with $j = 1, 2, 3, ...$, and

$$A_j = \left(\frac{2\omega_j^2 m_j}{V \varepsilon_0} \right)^{(1/2)}, \tag{1.27}$$

with $\omega_j = j\pi c/L$ being the cavity eigenfrequency, $V = LA$ (with A the transverse area of the optical resonator) is the volume of the resonator and m_j is a constant with mass dimension. The constant m_j has been included only to establish the analogy between the dynamical problem of a single mode of the electromagnetic field and that of the simple harmonic oscillator. The equivalent mechanical oscillator will have a mass m_j, and a Cartesian coordinate q_j. The nonvanishing component of the magnetic field H_y in

the cavity is obtained from Eq. (1.26):

$$H_y = \sum_j A_j \left(\frac{\dot{q}_j \varepsilon_0}{k_j} \right) \cos(k_j z). \tag{1.28}$$

The classical Hamiltonian for the field is

$$\mathcal{H} = \frac{1}{2} \int_V d^3x \left(\varepsilon_0 E_x^2 + \mu_0 H_y^2 \right) \tag{1.29}$$

where the integration is over the volume of the cavity. Substituting $\mathbf{E}_x$ and $\mathbf{H}_y$ of Eq. (1.29), by Eqs. (1.28) and (1.26), respectively, it follows that

$$\mathcal{H} = \frac{1}{2} \sum_j \left(m_j \omega_j^2 q_j^2 + m_j \dot{q}_j^2 \right) = \frac{1}{2} \sum_j \left(m_j \omega_j^2 q_j^2 + \frac{p_j^2}{m_j} \right) \tag{1.30}$$

where $p_j = m_j \dot{q}_j$ is the canonical momentum of the $j-th$ mode. Equation (1.30) expresses the Hamiltonian of the radiation field as a sum of independent oscillator energies. Each mode of the field is therefore dynamically equivalent to a mechanical harmonic oscillator.

1.4.1 Quantization of the electromagnetic field

The present dynamical problem can be quantized by identifying q_j and p_j as operators which obey the commutation relations

$$\left[\hat{q}_j, \hat{p}_{j'} \right] = i\hbar \delta_{jj'} \tag{1.31}$$

$$\left[\hat{q}_j, \hat{q}_{j'} \right] = \left[\hat{p}_j, \hat{p}_{j'} \right] = 0. \tag{1.32}$$

It is convenient to make a canonical transformation to operators $\hat{a}_j$ and $\hat{a}_j^\dagger$:

$$\hat{a}_j e^{-i\omega_j t} = \frac{1}{\sqrt{2m_j\hbar\omega_j}} \left(m_j\omega_j\hat{q}_j + i\hat{p}_j\right) \tag{1.33}$$

$$\hat{a}_j^\dagger e^{i\omega_j t} = \frac{1}{\sqrt{2m_j\hbar\omega_j}} \left(m_j\omega_j\hat{q}_j - i\hat{p}_j\right). \tag{1.34}$$

In terms of $\hat{a}_j$ and $\hat{a}_j^\dagger$, the Hamiltonian (Eq. (1.30)) becomes

$$\hat{\mathcal{H}} = \hbar\sum_j \omega_j \left(\hat{a}_j\hat{a}_j^\dagger + \frac{1}{2}\right). \tag{1.35}$$

The commutation relations between $\hat{a}_j$ and $\hat{a}_j^\dagger$ follow from those between q_j and p_j:

$$\left[\hat{a}_j, \hat{a}_{j'}^\dagger\right] = \delta_{jj'} \tag{1.36}$$

$$\left[\hat{a}_j, \hat{a}_{j'}\right] = \left[\hat{a}_j^\dagger, \hat{a}_{j'}^\dagger\right] = 0. \tag{1.37}$$

The operators $\hat{a}_j$ and $\hat{a}_j^\dagger$ referred to as the annihilation and the creation operators, respectively. In terms of $\hat{a}_j$ and $\hat{a}_j^\dagger$, the electric and magnetic fields (Eqs. (1.28) and (1.26) respectively) take the form:

$$\hat{E}_x(z,t) = \sum_j \mathcal{E}_j \left(\hat{a}_j e^{-i\omega_j t} + \hat{a}_j^\dagger e^{i\omega_j t}\right) \sin(k_j z) \tag{1.38}$$

$$\hat{H}_y(z,t) = -i\varepsilon_0 \sum_j \mathcal{E}_j \left(\hat{a}_j e^{-i\omega_j t} - \hat{a}_j^\dagger e^{i\omega_j t}\right) \cos(k_j z) \tag{1.39}$$

where the quantity $\mathcal{E}_j$ has the dimensions of an electric field:

$$\mathcal{E}_j = \left(\frac{\hbar\omega_j}{\varepsilon_0 V}\right)^{1/2}. \tag{1.40}$$

Until here, we have considered the quantization of the radiation field in a finite one-dimensional cavity. We can now quantize the field in unbounded free space as follows.

We consider the field in a large but finite cubic cavity of side L. Here we regard

the cavity merely as a region of space with no specific boundaries. We consider the running-wave solutions instead of the standing-wave solutions considered above and impose periodic boundary conditions.

The classical electric and magnetic fields can be expanded in terms of the plane waves

$$\mathbf{E}(\mathbf{r},t) = \sum_{\mathbf{k},s} \epsilon_{\mathbf{k},s}\mathcal{E}_{\mathbf{k}}\alpha_{\mathbf{k},s}e^{-i\omega_k t + i\mathbf{k}\cdot\mathbf{r}} + c.c. \tag{1.41}$$

$$\mathbf{H}(\mathbf{r},t) = \frac{1}{\mu_0}\sum_{\mathbf{k},s} \frac{\mathbf{k}\times\epsilon_{\mathbf{k},s}}{\omega_{\mathbf{k}}}\mathcal{E}_{\mathbf{k}}\alpha_{\mathbf{k},s}e^{-i\omega_k t + i\mathbf{k}\cdot\mathbf{r}} + c.c. \tag{1.42}$$

where the summation is taken over an infinite discrete set of values of the wave vector $\mathbf{k} \equiv (k_x, k_y, k_z)$, $\epsilon_{\mathbf{k},s}$ is a unit polarization vector, $\alpha_{\mathbf{k},s}$ is a dimensionless amplitude and

$$\mathcal{E}_{\mathbf{k}} = \left(\frac{\hbar\omega_k}{2\varepsilon_0 V}\right)^{1/2}. \tag{1.43}$$

In Eqs. (1.41) and (1.42) *c.c.* stands for complex conjugate. The periodic boundary conditions require that:

$$k_x = \frac{2\pi n_x}{L}, \quad k_y = \frac{2\pi n_y}{L}, \quad k_z = \frac{2\pi n_z}{L} \tag{1.44}$$

where n_x, n_y, n_z are integers $(0, \pm1, \pm2, ...)$. A set of numbers (n_x, n_y, n_z) defines a mode of the electromagnetic field. Equation 1.22 requires that:

$$\mathbf{k}\cdot\epsilon_{\mathbf{k},s} = 0 \tag{1.45}$$

i.e., the fields are purely transverse. There are, therefore, two independent polarization directions of $\epsilon_{\mathbf{k},s}$ for each $\mathbf{k}$.

The change from a discrete distribution of modes to a continuous distribution can

be made by replacing the sum in Eqs. (1.41) and (1.42) by an integral:

$$\sum_K \to 2\left(\frac{L}{2\pi}\right)^3 \int d^3k \tag{1.46}$$

where the factor 2 accounts for two possible states of polarization.

As before, the radiation field is quantized by identifying $\alpha_{\mathbf{k},s}$ and $\alpha^*_{\mathbf{k},s}$ with the harmonic oscillator operators $\hat{a}_{\mathbf{k},s}$ and $\hat{a}^\dagger_{\mathbf{k},s}$, respectively, which satisfy the commutation relation $\left[\hat{a}_{\mathbf{k},s}, \hat{a}^\dagger_{\mathbf{k},s}\right] = 1$.

The quantized electric and magnetic fields, including explicitly the two states of polarization denoted by the symbol s, become Hilbert space operators:

$$\hat{\mathbf{E}}(\mathbf{r},t) = \sum_{\mathbf{k},s} \epsilon_{\mathbf{k},s}\mathcal{E}_{\mathbf{k}}\hat{a}_{\mathbf{k},s}e^{-i\omega_k t + i\mathbf{k}\cdot\mathbf{r}} + H.c. \tag{1.47}$$

$$\hat{\mathbf{H}}(\mathbf{r},t) = \frac{1}{\mu_0}\sum_{\mathbf{k},s} \frac{\mathbf{k}\times\epsilon_{\mathbf{k},s}}{\omega_{\mathbf{k}}}\mathcal{E}_{\mathbf{k}}\hat{a}_{\mathbf{k},s}e^{-i\omega_k t + i\mathbf{k}\cdot\mathbf{r}} + H.c. \tag{1.48}$$

where $H.c.$ stands for Hermitian conjugate. Usually the field operators can be decomposed into its positive-frequency and negative-frequency parts. For example, the electric field operator $\hat{\mathbf{E}}(\mathbf{r},t)$ is written as:

$$\hat{\mathbf{E}}(\mathbf{r},t) = \hat{\mathbf{E}}^{(+)}(\mathbf{r},t) + \hat{\mathbf{E}}^{(-)}(\mathbf{r},t) \tag{1.49}$$

where $\hat{\mathbf{E}}^{(+)}(\mathbf{r},t)$ contains only the annihilation operators and its adjoint $\hat{\mathbf{E}}^{(-)}(\mathbf{r},t)$ contains only the creation operators.

An important consequence of imposing the quantum conditions of Eqs. (1.36) and (1.37) is that, as the electric and magnetic field strengths do not commute, they are thus not measurable simultaneously.

The corresponding commutation relations between the operators $\hat{a}_{\mathbf{k},s}$ and $\hat{a}^\dagger_{\mathbf{k},s}$ are:

$$\left[\hat{a}_{\mathbf{k},s}, \hat{a}_{\mathbf{k}',s'}\right] = \left[\hat{a}^\dagger_{\mathbf{k},s}, \hat{a}^\dagger_{\mathbf{k}',s'}\right] = 0 \tag{1.50}$$

$$\left[\hat{a}_{\mathbf{k},s}, \hat{a}^\dagger_{\mathbf{k}',s'}\right] = \delta_{\mathbf{k}\mathbf{k}'}\delta_{ss'}. \tag{1.51}$$

It follows that the equal time commutators relations between the field components are given by [36]:

$$\left[\hat{\mathbf{E}}_j(\mathbf{r},t),\hat{\mathbf{H}}_j(\mathbf{r}',t)\right]=0 \quad (j=x,y,z), \tag{1.52}$$

$$\left[\hat{\mathbf{E}}_j(\mathbf{r},t),\hat{\mathbf{H}}_k(\mathbf{r}',t)\right]=-i\hbar c^2\frac{\partial}{\partial l}\delta^{(3)}(\mathbf{r}-\mathbf{r}') \tag{1.53}$$

where j, k, and l form a cyclic permutation of x, y, and z.

We, therefore, conclude that the parallel components of $\hat{\mathbf{E}}$ and $\hat{\mathbf{H}}$ may be measured simultaneously whereas the perpendicular components cannot.

1.4.2 Fock number states

In this section we first restrict ourselves to a single mode of the field of frequency ω having creation and annihilation operators $\hat{a}$ and $\hat{a}^\dagger$, respectively. Let $|n\rangle$ be the energy eigenstate corresponding to the energy eigenvalue E_n:

$$\mathcal{H}|n\rangle=\hbar\omega\left(\hat{a}^\dagger\hat{a}+\frac{1}{2}\right)|n\rangle=E_n|n\rangle. \tag{1.54}$$

If we apply the operator $\hat{a}$ from the left, we obtain after using the commutation relation $\left[\hat{a},\hat{a}^\dagger\right]=1$ and some rearrangement

$$\mathcal{H}|n-1\rangle=\mathcal{H}\hat{a}|n\rangle=\left(E_n-\hbar\omega\right)\hat{a}|n\rangle. \tag{1.55}$$

This means that the state $|n-1\rangle\propto\hat{a}|n\rangle$, is also an energy eigenstate but with the reduced eigenvalue, $E_{n-1}=E_n-\hbar\omega$.

If we repeat this procedure n times we move down the energy ladder in steps of $\hbar\omega$ until we obtain $\mathcal{H}\hat{a}|0\rangle=\left(E_0-\hbar\omega\right)\hat{a}|0\rangle$. Here E_0 is the ground state energy such that $(E_0-\hbar\omega)$ would correspond to an energy eigenvalue smaller than E_0. Since we do not allow energies lower than E_0 for the oscillator, we must conclude that $\hat{a}|0\rangle=0$.

The state $|0\rangle$ is referred to as the vacuum state and the value of the zero point of

energy is:

$$E_0 = \frac{1}{2}\hbar\omega. \tag{1.56}$$

It then follows that:

$$E_n = \left(n + \frac{1}{2}\right)\hbar\omega. \tag{1.57}$$

From Eq. 1.54, we obtain $\hat{a}^\dagger\hat{a}|n\rangle = \hat{n}|n\rangle$, i.e. the energy eigenstate $|n\rangle$ is also eigenstate of the 'number' operator $\hat{n} = \hat{a}^\dagger\hat{a}$.

Now, we can easily obtain the fundamental equations [36]

$$\hat{a}|n\rangle = \sqrt{n}|n-1\rangle, \tag{1.58}$$

$$\hat{a}^\dagger|n\rangle = \sqrt{n+1}|n+1\rangle. \tag{1.59}$$

It is useful to interpret the energy eigenvalues (Eq. (1.57)) as corresponding to the presence of n photons of energy $\hbar\omega$. The eigenstates $|n\rangle$ are called Fock states or photon number states. They form a complete set of states, i.e.,

$$\sum_{n=0}^{\infty} |n\rangle\langle n| = 1. \tag{1.60}$$

The energy eigenvalues are discrete, in contrast to classical electromagnetic theory where energy can have any value. The energy expectation value can however take on any value, for the state vector is, in general, an arbitrary superposition of energy eigenstates, i.e.,

$$|\psi\rangle = \sum_n c_n|n\rangle \tag{1.61}$$

where c_n are complex coefficients.

An important property of the number state $|n\rangle$ is that the corresponding expectation value of the single-mode linearly polarized field operator

$$\hat{\mathbf{E}}(\mathbf{r},t) = \mathcal{E}\hat{a}e^{-i\omega_k t + i\mathbf{k}\cdot\mathbf{r}} + H.c. \tag{1.62}$$

vanishes, i.e.

$$\langle n|\hat{\mathbf{E}}|n\rangle = 0 \tag{1.63}$$

However, the expectation value of the intensity operator $\hat{\mathbf{E}}^2$ is given by

$$\langle n|\hat{\mathbf{E}}^2|n\rangle = 2|\mathcal{E}|\left(n+\frac{1}{2}\right) \tag{1.64}$$

i.e., there are fluctuations in the field about its zero ensemble average. It is interesting to note that there are nonzero fluctuations even for a vacuum state $|0\rangle$. These vacuum fluctuations are responsible for many interesting phenomena in quantum optics, for example it may be considered that they stimulate the spontaneous decay of a photon pump field in photon pairs in the process of PDC.

The operators $\hat{a}$ and $\hat{a}^\dagger$ annihilate and create photons respectively, as seen in Eqs. (1.58) and (1.59) they change a state with n photons into one with $n-1$ or $n+1$ photons. The operators $\hat{a}$ and $\hat{a}^\dagger$ are therefore referred to as annihilation (or destruction) and creation operators, respectively. These operators are not themselves Hermitian ($\hat{a} \neq \hat{a}^\dagger$) and do not represent observable quantities such as the electric and magnetic field amplitudes. However, some combinations of the operators are Hermitian such as quadrature operators $\hat{X} = (\hat{a}+\hat{a}^\dagger)/2$, $\hat{Y} = (\hat{a}-\hat{a}^\dagger)/2i$.

So far we have considered a single-mode field and have found that, in general, the wave function can be written as a linear superposition of photon number states . This formalism can be easily extended to multi-mode fields.

1.4.3 Two-photon wave function

A theoretical study of the process of parametric down-conversion is presented in this section. We use a simple Hamiltonian model to describe the coupling of the incident pump field to the down-converted signal and idler fields over a region that coincides with the volume of the nonlinear medium. The down-converted fields are decomposed into an infinite set of modes, which is eventually treated as a continuum. According to Section 1.1, in a nonlinear dielectric medium an incident field $\mathbf{E}$ will create a polarization $\mathbf{P}$

presenting contributions that are at least bilinear in **E**. The lowest order non-linearity is the bilinear supsceptibility $2d_{ijl}$. This makes a contribution to the energy of the electromagnetic field of the form

$$\mathcal{H}_I(t) = 2\varepsilon_0 \int_{\mathcal{V}} 2d_{ijl} E_i(\mathbf{r},t) E_j(\mathbf{r},t) E_l(\mathbf{r},t) d^3x \tag{1.65}$$

$$\tag{1.66}$$

where the interaction extends over the volume $\mathcal{V}$ of the nonlinear medium, and E_m are the components of the vector **E** for the three interacting fields. The two quantized down-converted fields are described as:

$$\hat{\mathbf{E}}(\mathbf{r},t) = \sum_s \int \epsilon_s \mathcal{E}_{\mathbf{k}} \hat{a}_{\mathbf{k},s} e^{i(\mathbf{k}\cdot\mathbf{r}-\omega t)} d^4k + H.c. \tag{1.67}$$

where the $d^4k = d^3k\ d\omega$, and the relation between k and ω is $\frac{\omega}{|k|} = \frac{c}{n}$. In the next, it is assumed that the incident field is so intense that it can be treated classically. This is an approximation, but one that is usually acceptable for the laser beam, as long as the beam is only weakly attenuated in passing through the non linear medium. Then, the expression for the pump radiation, that is a monochromatic field in the z direction and with a defined polarization, is:

$$\mathbf{E}_p(\mathbf{r},t) = \vec{\epsilon}_{s_p} \mathcal{E}_{\mathbf{k}_p} \alpha_{\mathbf{k}_p,s_p} e^{i(\mathbf{k}_p\cdot z-\omega_p t)} + c.c.. \tag{1.68}$$

According with Eqs. (1.67) and (1.68), the Hamiltonian (1.65) becomes [37]

$$\begin{aligned}\mathcal{H}_I(t) = 2\varepsilon_0 \int_{\mathcal{V}} \chi^{(2)}_{ijl} \sum_{s's''} \int\int (\epsilon_{s_p})_i (\epsilon_{s'})_j (\epsilon_{s''})_l \mathcal{E}_{\mathbf{k}_p} \mathcal{E}_{\mathbf{k}'} \mathcal{E}_{\mathbf{k}''} \alpha_{\mathbf{k}_p,s_p} \hat{a}^\dagger_{\mathbf{k}',s'} \hat{a}^\dagger_{\mathbf{k}'',s''} \\ e^{i(k_p-k'_z-k''_z)z} e^{-i(\vec{q}\,'+\vec{q}\,'')\cdot\vec{\rho}} e^{-i(\omega_p-\omega'-\omega'')t}\ d\omega'\ d\omega''\ d^2q'\ d^2q''\ dz\ d^2\rho + H.C.\end{aligned} \tag{1.69}$$

where $\mathbf{k}' = k'_z\hat{e_z} + \vec{q}\,'$, $\mathbf{k}'' = k''_z\hat{e_z} + \vec{q}\,''$, $\mathbf{r} = z\hat{e_z} + \vec{\rho}$ and k_z and ω are related by $k_z = \sqrt{\left(\frac{\omega}{c}n(\omega)\right)^2 - |\vec{q}|^2}$.

The parametric down conversion two-photon state in the interaction picture is given

by [38–40]:

$$|\psi\rangle = exp\left[\frac{1}{i\hbar}\int_{-\infty}^{+\infty}\mathcal{H}_I(t')dt'\right]|0\rangle = \left[1-\frac{1}{i\hbar}\int_{-\infty}^{\infty}\mathcal{H}_I(t')dt'\right]|0\rangle \tag{1.70}$$

By introducing Eq. (1.69) in Eq. (1.70) and solving the time integral a Dirac delta function is obtained $\delta(-\omega_p+\omega^{'}+\omega^{''})$ and the frequency phase matching condition $\omega_p=\omega^{'}+\omega^{''}$ is recovered.

When the integral over the volume $\mathcal{V}$ of the crystal is performed, we have to distinguish between the integral in the pump propagation direction z and the integral in the transverse direction ρ. When considering the crystal infinite in the transversal direction, the integral over the area A of the intersection of the beam cross section and the crystal gives

$$\int_A e^{i(\vec{q}\,'-\vec{q}\,'')\cdot\vec{\rho}}\,d^2\rho = \delta(\vec{q}\,'+\vec{q}\,'') \tag{1.71}$$

In this approximation, the modes are correlated in pairs. Each signal photon with $\mathbf{k}'=\vec{q}\,'+k_z'\hat{e}_z$ is correlated with an idler photon with $\mathbf{k}''=-\vec{q}\,'+k_z''\hat{e}_z$.

Considering L the length of the crystal, the space integral in the z direction is

$$\int_{-L/2}^{L/2} e^{i(k_p-k_z'-k_z'')\cdot\hat{z}}dz = sinc\left((k_p-k_z'-k_z'')L/2\right) \tag{1.72}$$

Finally, the expression for the biphoton-field state can be rewritten as:

$$\begin{aligned}|\psi\rangle = |0\rangle - \frac{2\varepsilon_0}{i\hbar}\Bigg\{\sum_{s's''}\int \chi^{(2)}_{ijl}(\epsilon_{s_p})_i(\epsilon_{s'})_j(\epsilon_{s''})_l\mathcal{E}_{\mathbf{k}_p}\mathcal{E}_{(\mathbf{q}',\omega')}\mathcal{E}_{(\text{-}\mathbf{q}',\omega_p-\omega')}\\ sinc\left[\left(k_p-k_z'-k_z''\right)L/2\right]\alpha_{\mathbf{k}_p,s_p}\hat{a}^\dagger_{(\mathbf{q}',\omega',s')}\hat{a}^\dagger_{(\text{-}\mathbf{q}',\omega_p-\omega',s'')}d\omega'\,d^2q' + H.C.\Bigg\}|0\rangle\end{aligned} \tag{1.73}$$

where $k_z'=\sqrt{\left(\frac{\omega'}{c}n(\omega')\right)^2-|\vec{q}\,'|^2}$ and $k_z''=\sqrt{\left(\frac{\omega_p-\omega'}{c}n(\omega_p-\omega')\right)^2-|\vec{q}\,'|^2}$.

1.4.4 Multi-photon wave function

In this section the expression for the multi-photon wave function in the PDC process will be found, starting from the expression of the state vector of Eq. (1.70). In this case, this equation will be solved completely, without using a perturbative approximation.

Initially, the temporal integral of Eq. (1.70) is solved and, as in the two-photon case, a Dirac delta $\delta(-\omega_p + \omega' + \omega'')$ is obtained. The spatial integral in the transverse direction to the pump propagation is calculated, achieving the same result of Eq. (1.71). For the space integral in the pump propagation direction, the length of the crystal is considered very large and approximately infinite, then the integral over z becomes:

$$\int_{-\infty}^{+\infty} e^{i(k_p - k'_z - k''_z)\cdot\hat{z}} dz = 2\pi\ \delta(k_p - k'_z - k''_z) \tag{1.74}$$

from which the momentum phase matching condition is recovered. Introducing this results in the main equation (Eq. (1.70)), the multi-photon wave function becomes:

$$\begin{aligned} |\psi\rangle &= exp\left[\frac{-i}{\hbar}\int_{-\infty}^{+\infty} H_I dt\right]|0\rangle \\ &= exp\left[\sum_{s's''}\int \zeta(\mathbf{q}', \omega', s', s'')\hat{a}^{\dagger}_{(\mathbf{q}',\omega',s')}\hat{a}^{\dagger}_{(-\mathbf{q}',\omega_p-\omega',s'')} d\omega' d^2q' - H.C.\right]|0\rangle \end{aligned} \tag{1.75}$$

with

$$\zeta(q', \omega', s', s'') = \frac{-i4\pi\varepsilon_0}{\hbar}\chi^{(2)}_{ijl}(\epsilon_{s_p})_i(\epsilon_{s'})_j(\epsilon_{s''})_l \mathcal{E}_{\mathbf{k}_p}\mathcal{E}_{(\mathbf{q}',\omega')}\mathcal{E}_{(\mathbf{-q}',\omega_p-\omega')}\alpha_{k_p,s_p}. \tag{1.76}$$

rewriting this integrals on q' and ω' as summation over the corresponding (discretized) variables Q' and Ω' we obtain:

$$|\psi\rangle = exp\left[\sum_{s's''\Omega'Q'} \zeta(Q', \Omega', s', s'')\hat{a}^{\dagger}_{(\mathbf{Q}',\Omega',s')}\hat{a}^{\dagger}_{(-\mathbf{Q}',\Omega_p-\Omega',s'')} - H.C.\right] \tag{1.77}$$

By using the Campbell-Baker-Hausdorff theorem [41], that claims that for two com-

muting operators $\hat{A}$ and $\hat{B}$ holds:

$$e^{x(\hat{A}+\hat{B})} = e^{x\hat{A}}e^{x\hat{B}} \tag{1.78}$$

and observing that the commutator

$$\begin{aligned}\Big[&\zeta(Q'_0,\Omega'_0,s',s'')\hat{a}^{\dagger}_{(\mathbf{Q}'_0,\Omega'_0,s')}\hat{a}^{\dagger}_{(-\mathbf{Q}'_0,\Omega_p-\Omega'_0,s'')} - H.C.\ ;\\ &\zeta(Q',\Omega',s',s'')\hat{a}^{\dagger}_{(\mathbf{Q}',\Omega',s')}\hat{a}^{\dagger}_{(-\mathbf{Q}',\Omega_p-\Omega',s'')} - H.C.\Big] = 0\end{aligned} \tag{1.79}$$

for all $Q'_0 \neq Q'$ and $\Omega'_0 \neq \Omega'$, (see Eq. (1.50)), we can rewrite Eq. (1.77) as:

$$|\psi\rangle = \bigotimes_{s's''\Omega'Q'} exp\left[\zeta(Q',\Omega',s',s'')\hat{a}^{\dagger}_{(\mathbf{Q}',\Omega',s')}\hat{a}^{\dagger}_{(-\mathbf{Q}',\Omega_p-\Omega',s'')} - H.C.\right]|0\rangle = \bigotimes_{q}|\psi\rangle_q \tag{1.80}$$

It is possible to write $|\psi\rangle_q$ in terms of the average number of generated photons per mode μ:

$$|\psi\rangle_q = \sum_n c_n |n\rangle_{q_A}|n\rangle_{q_B} \tag{1.81}$$

where

$$c_n = \frac{1}{\sqrt{1+\mu}}\left(\sqrt{\frac{\mu e^{i\theta}}{1+\mu}}\right)^n \tag{1.82}$$

and $\mu = senh^2(r)$, where $r = |\zeta|$ and $\zeta = re^{i\theta}$.

Chapter 2

Single photon detector calibration

2.1 Absolute calibration exploiting parametric down conversion correlations

The PDC process is used to create the correlated pair of photons that allow the absolute determination of detector quantum efficiency to be made. In PDC process (see section 1.3) there is a small probability that a pump photon impinging in a $\chi^{(2)}$ nonlinear crystal to decay into a pair of lower frequency photons. This decay is constrained by conservation of energy and momentum (phase matching conditions)

$$\omega_p = \omega_s + \omega_i; \quad \mathbf{k}_p = \mathbf{k}_s + \mathbf{k}_i \tag{2.1}$$

were ω_p, ω_s and ω_i are pump, signal and idler frequencies and $\mathbf{k}_p$, $\mathbf{k}_s$ and $\mathbf{k}_i$ are pump, signal and idler wave vectors respectively. Because of the constraints of simultaneous creation of a pair of photons, the knowledge of the pump beam and one of the output photons provides information about its mate. Specifically it announces not only the existence of the second photon, but although the emission time, wavelength, direction of propagation and polarization of one of them tell all about the other. The non detection of the announced photon is due to the non ideal quantum efficiency of the detector under calibration, which can be measured in this way. The simultaneous creation of the two

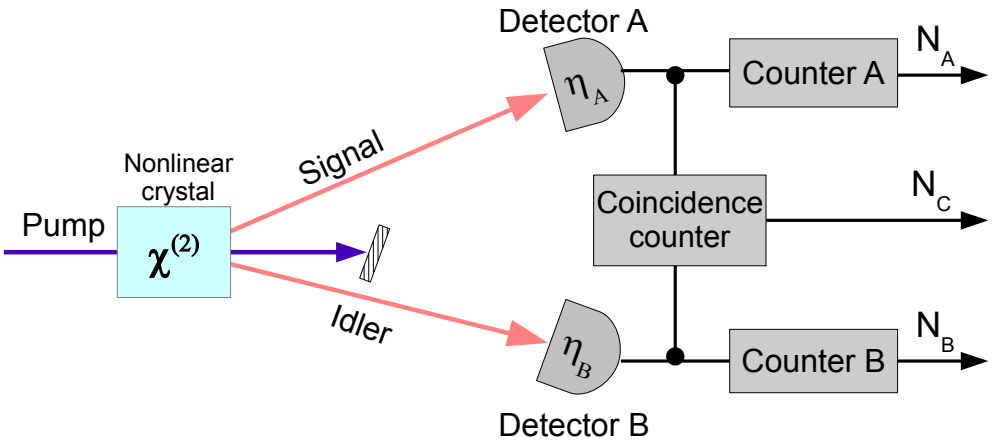

Figure 2.1: Scheme for absolute calibration of a photon detector. PDC photons are generated in a non-linear crystal pumped by a laser. Detector A and detector B (with efficiency η_A and η_B) collects the photons of correlated channels. The number of signal and ideler counts (N_A and N_B) and the number of photons arriving in coincidence to both detectors (N_C) are obtained by using counters and coincidence electronics.

photons allows an absolute measurement of the detection efficiency without the support of an external calibrated radiometric standard [42–45].

If the phase matching conditions are applied to a particular crystal, it is possible to generate non collinear signal and idler photons pairs, that allows an easy optical discrimination and makes these photon pairs useful for measure the quantum efficiency of photodetectors operating in the photon counting regime.

The calibration of single photon detectors described in this thesis is based in the Klyshko method [42]. In Fig 2.1 a scheme of the Klyshko's calibration technique is shown. A pump laser impinges on a non linear crystal, generating PDC photons. Two correlated channels of emission corresponding to a signal and idler photon propagation direction are selected and directed to photo counters A and B (with efficiencies η_A and η_B) respectively.

If one photon of the pair is detected, the presence of the second photon along the correlated direction is ensured. Considering a given time interval, let us nominate the total number of pairs emitted by the crystal as N, the average count rate recorded by detectors A and B during the same time interval N_A and N_B respectively, and the

coincidences (i.e. the events corresponding to simultaneous counts from both detectors, due to the detection of PDC photon pair) count rate as N_C, then we have the relations:

$$\begin{aligned} N_A &= \eta_A(\lambda_A)N \\ N_B &= \eta_B(\lambda_B)N \end{aligned} \tag{2.2}$$

where $\eta_A(\lambda_A)$ and $\eta_B(\lambda_B)$ are the detection efficiencies of photodetectors A and B at specific wavelength λ_A and λ_B. The statistical independence of the detectors, allow us to express the number of coincidences as:

$$N_C = \eta_A(\lambda_A)\eta_B(\lambda_B)N \tag{2.3}$$

then, the detection efficiency can be obtained as:

$$\begin{aligned} \eta_A(\lambda_A) &= \frac{N_C}{N_B} \\ \eta_B(\lambda_B) &= \frac{N_C}{N_A} \end{aligned} \tag{2.4}$$

This simple relation is the basis for the scheme of absolute calibration of single photon detectors by means of PDC.

Nevertheless, in practice it is not easy to assure that both detectors see only correlated photons thus, in order to measure the coincidences, it is necessary to broke the symmetry and associate each channel with a different role: one detector act as a trigger, while the other is the device under test (DUT). The trigger announces the existence of a photon of the pair in the DUT channel, with certain probability of being detected by the DUT. Then, for every detection in the trigger we look to see if there is, in coincidence, a photon detected at DUT. Note, that the determination of the DUT quantum efficiency (η_{DUT}) is independent of the trigger efficiency. Some photons arriving to the trigger will not be detected, since the trigger has not efficiency equal to one, i.e. the trigger is not perfect, but this does not affect the DUT calibration.

Although there are some subtleties that will be discussed in the next sections, this technique is intrinsically absolute in the sense that no reference standards are needed.

The technique exploits only the spatial and temporal correlation between twin photons generated by PDC.

2.2 Experimental setup

In the next subsections a complete description of the experimental apparatus is introduced. In the first part a description of the optical setup that is used in the detector quantum efficiency measurement is presented. In the second part a detailed explanation of the electronic that is used to count photons and coincidences is given.

2.2.1 Optical setup

The arrangement for the quantum efficiency calibration is shown in Figure 2.2. A continuous wave linearly polarized argon laser, working at 351 nm wavelength, is used to pump a 10 mm long β-barium borate (BBO) crystal cut for Type I SPDC phase matching (signal and idler are emitted with the same polarization and in concentric cones of different wavelengths). The crystal has a cutting angle of 33.4 ° and a coating AR/AR 351/351. To avoid back reflections, the crystal is placed such that the pump has no normal incidence and the effective cutting angle is 33.9 °. After the crystal, the remaining UV radiation not converted is stopped. A first half-waveplate ($\lambda/2$) and a polarizer are used to control the pump power. A second half-waveplate is placed between the polarizer and the crystal to allow the rotation of the pump beam polarization, giving the possibility to turn on and off the PDC process (because the phase matching conditions permits only one pump polarization to be down converted). By suppressing the PDC process the dark counts rate are measured.

The trigger and the DUT detectors are Avalanche Photo Diode (APD) based single photon counting modules (SPCM-AQR-15, serial number 4916-1 and 4915-1 respectively) with an active area of 175 μm diameter. To properly position the detectors, the output angles and angular dispersion of the working wavelength are estimated, using the NIST Phasematch program, to be 3.7 ° and 0.01 ° nm for radiation at 761 nm and 3.15 °

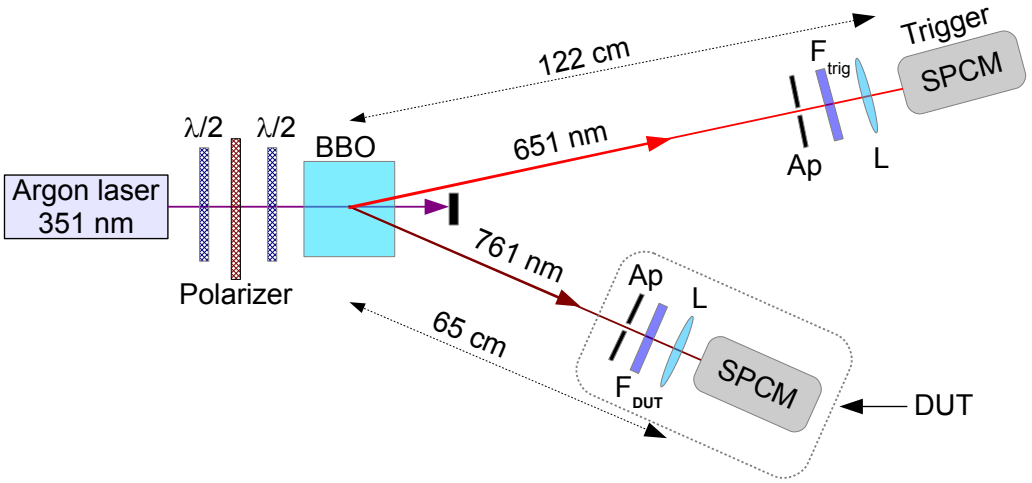

Figure 2.2: Experimental setup for absolute quantum efficiency measurement using type I PDC at 761 nm (DUT) and 651 nm (trigger) generated in a BBO crystal. The first half wave plate ($\lambda/2$) and polarizer are used for pump attenuation, while the second half wave plate is used to suppress the PDC generation. Both trigger and DUT are single photon counting modules SPCM-AQR-15. The DUT efficiency is considered as the efficiency of the DUT detector and its optics as a unit. An aperture (Ap) is used to limit the collection area of each detector, while F_{trig} is a 3 nm FWHM interference filter centered at 651 nm and the F_{DUT} is a 20 nm FWHM interference filter at 761 nm. A lens (L) is used to focus the light in each detector active area.

and 0.005 ° nm for radiation at 651 nm. The trigger and DUT detectors are positioned at a distance of 122 cm and 65 cm respectively from the centre of the crystal.

A device specially designed in the lab to mount in front of each detector is used to house three components: a lens, an interference filter and an aperture. The mounting allow the movement of the lens axially, changing the focus position, in order align it. Before the lens an interference filter with maximum transmittance at 651 nm (69.3 %) and bandwidth 3 nm FWHM is used to select the proper wavelength of parametric fluorescence emission on the trigger channel. On DUT arm an interference filter with transmittance of about 65 % at 761 nm and bandwidth 20 nm FWHM is used. The aperture, an iris with variable diameter from 2 mm to 12 mm, is mounted to control the collection area of the detectors. Note that, due to the divergence of the PDC light, the aperture makes a spatial selection of the light wavelength, in addition to the spectral selection made by the interference filters.

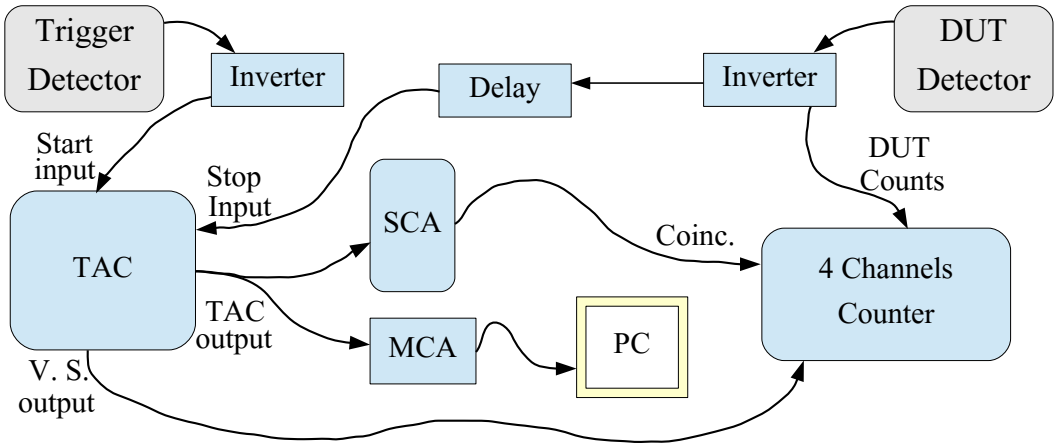

Figure 2.3: Electronics setup. The output signal pulses of the detectors are inverted and properly delayed and sent to the TAC. The TAC outputs are sent to a MCA and to a SCA. TAC valid start output (V.S.), coincidence counts and DUT raw counts are measured by the counter. The whole measurement system is controlled by a PC.

2.2.2 Electronics

A complete scheme of the electronics of this experiment can be seen in Figure 2.3. To perform coincidence measurements the Time to Amplitude Converter / Single Channel Analyzer module (TAC/SCA) is commonly used. The TAC circuit converts time intervals between a start and a stop signal in electrical pulses with an amplitude proportional to the time separation between pulses at its start and stop inputs.

The start input signal of the TAC is provided by the output signal of the trigger detector, while the stop signal is given by the DUT detector output delayed (6.5 ns). The TAC output is sent simultaneously to a multichannel analyzer (MCA) and to a single-channel analyzer (SCA). The MCA records histograms of inter-arrival times of the DUT and trigger events. Correlated photon pairs are seen in the histogram as a peak whose width is due to the combined time jitter of the detectors and the electronics as shown in Figure 2.4. The SCA circuit gives a logic signal for each arriving pulse in an operator selected time interval (in this experiment, the SCA window is set in 7.7 ns). The SCA output is addressed to a counter in order to measure coincidence counts.

Correlated photon pairs are seen in the histogram as a peak on top of a flat back-

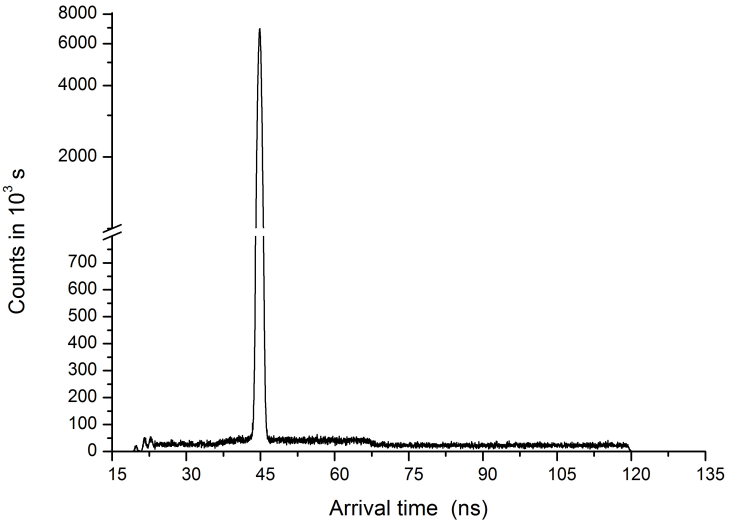

Figure 2.4: Histogram recorded by the MCA showing the inter arrival time of the trigger and DUT events. Uncorrelated counts are seen as a flat background, while the correlated photon pairs are observed as a peak.

ground resulting from uncorrelated output pulses from the two detectors. True coincidences are found by counting the events within a fixed time window around this peak and subtracting the flat background level within the same time window (referred to as accidental coincidences). The coincidence window must be set wide enough to contain all the true coincidences: to achieve uncertainties well much below 1%, it must be set many times the FWHM of the coincidence peak [46], due to long tails of the peak. Accidental coincidence counts can be measured by an insertion of a further 24 ns delay in DUT channel, much greater than the coincidence circuits resolving time.

For the quantum efficiency measurements here presented we use a TAC-SCA Canberra Model 2145 equipped with a "valid start output" providing valid trigger events (photons arriving to the detector within the electronic's dead time are not count as a valid start signal), whose single counts are measured by an EG&G Ortec Quad Counter-Timer Model 974. The automatic measurement system is fully PC controlled by GPIB interface card. The positive pulses generated by the photon counters are inverted in order to be processed by the above described NIM electronics.

2.3 Measurement procedure

To account for the presence of unwanted counts the simple formula 2.4 given in section 2.1 has to be modified. In addition to the correlated photons, each detector suffers of background counts, due to unwanted external light (e.g. stray light or unheralded PDC light), and spurious counts due to thermal fluctuation inside the detector or trapped carriers (dark counts and after pulses). Thus, because of the finite duration of the coincidence window, spurious coincidence counts are superimposed on the correlated pairs, leading to the above mentioned background counts and accidental coincidences. To correct for the unwanted detected light, the measured quantum efficiency, η_{DUT}^{meas}, is estimated from [44, 47, 48]

$$\eta_{DUT}^{meas} = \frac{\langle m_c \rangle - \langle A \rangle}{\langle m_{vs} \rangle - \langle m_B \rangle} \tag{2.5}$$

where the "$\langle\ \rangle$" represent the average over a fixed time of: the coincidence counts measured by TAC/SCA (m_c), the valid start counts (m_{vs}), the background counts on the valid start (m_B) and the accidental coincidence counts (A).

Concerning this last correction one has to detail a little more about the evaluation of the dark counts or accidental coincidences $\langle A \rangle$. The TAC valid start output provides only the true trigger events, i.e. counts arriving when the detector is "alive", not during its dead time. Only this true trigger events are considered for conversion and give contribution to coincidences. Thus the TAC dead time effect can be neglected thanks to the valid start output. We should also note that the number of valid start counts able to produce an accidental coincidence drastically changes if the peak of coincidences is in the SCA windows or not. Because the accidental counts are evaluated by adding a delay to the DUT output, in order to move the peak out of the measurement window, a correction for $\langle A \rangle$ should be added accounting to this valid start mismatch. A reasonable first order correction is given by

$$\langle A' \rangle \cong \langle A \rangle \frac{\langle m_{vs}^{in} \rangle}{\langle m_{vs}^{out} \rangle} \tag{2.6}$$

where $\langle m_{vs}^{in} \rangle$ is the average of the valid start counts when the coincidence peak is in the SCA window and $\langle m_{vs}^{out} \rangle$ is valid start average when the coincidence peak is not in the SCA windows.

The measured quantum efficiency accounting this correction is then

$$\eta_{DUT}^{meas'} = \frac{\langle m_c \rangle - \langle A \rangle \frac{\langle m_{vs}^{in} \rangle}{\langle m_{vs}^{out} \rangle}}{\langle m_{vs}^{in} \rangle - \langle m_B \rangle} \tag{2.7}$$

If we take into account a correction due to optical losses, we obtain the quantum efficiency of just the detector under calibration

$$\eta_{DUT} = \frac{1}{\tau_{DUT}} \eta_{DUT}^{meas'} \tag{2.8}$$

where τ_{DUT} is the total transmittance of the DUT channel.

The number of DUT counts, m_{DUT}^{meas}, measured over a time interval T, is less than the effective number of counts m_{DUT}, because of the dead time, t_D, of the DUT detector. If we assume a non-extended dead time for DUT, as it is the case of Perkin Elmer detector, the effective mean counts are approximately [15]

$$\langle m_{DUT} \rangle \cong \frac{\langle m_{DUT}^{meas} \rangle}{(1 - \langle m_{DUT}^{meas} \rangle \frac{t_D}{T})} \tag{2.9}$$

and the model for quantum efficiency with the dead time correction is then

$$\eta_o \cong \frac{\eta_{DUT}}{(1 - \langle m_{DUT}^{meas} \rangle \frac{t_D}{T})} \tag{2.10}$$

Thus the formula for the quantum efficiency estimation with all the above mention correction accounted for is

$$\eta_o \cong \frac{1}{(1 - \langle m_{DUT}^{meas} \rangle \frac{t_D}{T})} \frac{1}{\tau_{DUT}} \frac{\langle m_c \rangle - \langle A \rangle \frac{\langle m_{vs}^{in} \rangle}{\langle m_{vs}^{out} \rangle}}{\langle m_{vs}^{in} \rangle - \langle m_B \rangle} \tag{2.11}$$

2.3.1 PDC light focusing

A lens is mounted in front of each detector to focus the PDC light into the sensitive surface of the SPCM. The mounting allow the movement of the lens axially to change the focus position. A 633 nm laser is attenuated using neutral filters to reduce the power down to the single photon regime. With the attenuated laser the lens of the trigger arm is moved to maximize the trigger detector counts, focusing the light in the detector active area. With a similar procedure a 789 nm is used to align the DUT lens. The wavelengths that are used to the lens alignment are the closer ones to the idler and signal desired photons available in the labs. This difference in the wavelength do not affect the procedure and the collimation position is verified before the measurements once the PDC light is found.

2.3.2 Detector alignment

In practice, it is not easy to select exactly the same number of correlated photons in both channels. Different tricks are used to make both spatial and spectral selection of the PDC light at the desired wavelength, and ensure a total collection of the photon pairs.

Taking advantage of the divergence of the PDC light, and because both detectors have the same detection area, a first spatial selection is made by placing the DUT and trigger detector at different distances from the PDC source, see Figure 2.5. Thus, the DUT is placed near from the source than the trigger detector, facilitating the complete collection of the corresponding twin photons in the DUT arm. In our configuration the trigger detector is placed at 122 cm from the crystal and DUT at 65 cm.

In addition, in each channel, a spectral selection is obtained using interference filters, and a second spatial selection is made using a adjustable iris. For the trigger channel a short range of wavelength, defined by a narrower bandwidth interference filter 3 nm and an iris are used to properly select the fluorescence, while for the DUT channel the spectral bandpass and collection iris are larger, ensuring that all the photons correlated to those arriving to the trigger fall on DUT.

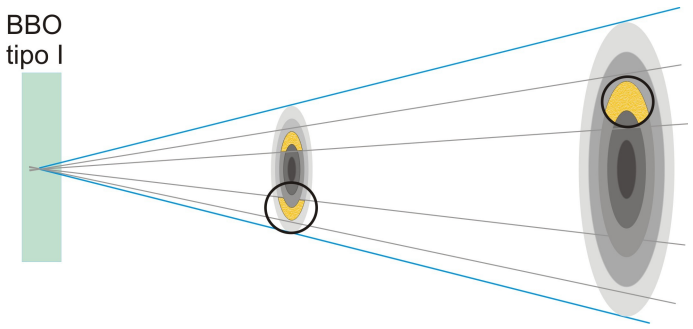

Figure 2.5: Due to the divergence of the PDC light and because both detectors have the same collection area (black circles), the trigger detector is placed farther from the source, making a spatial selection and facilitating the complete collection of the corresponding twin photons in the DUT channel. In the figure the yellow area corresponds to the correlated photons between the two detectors.

To properly align the detector it is necessary to estimate first the output angles of the desired PDC radiation. As mention in section 2.2.1, the Phase Match program of NIST [49] is used to estimate the emission direction. For the conditions of this experiment the estimation gives an output angle of 3.5 ° for radiation at 651 nm (trigger) and 3.7 ° for radiation at 761 nm (DUT).

In the alignment procedure the trigger detector is first positioned where the 651 nm radiation is expected to be seen. Because the detector package includes a collection lens it is necessary to do an iterative optimization of its translational position and its angular orientation in order to maximize the single photon counts. This centres the detector in the central wavelength of the spectral filter.

The DUT must then be centred radially and tangentially along down-converted light cone on the light correlated to the trigger. The procedure to centre the DUT on the correlated beam involves iterative optimization of its translational position and its angular orientation maximizing the coincidences counts. This procedure consists of stopping down the collection lens iris before translational maximization of the correlated signal. Then the detector/lens package is tilted about the lens position allowing the detector to be positioned at the focused spot of light. These two steps are repeated until no further gains are seen.

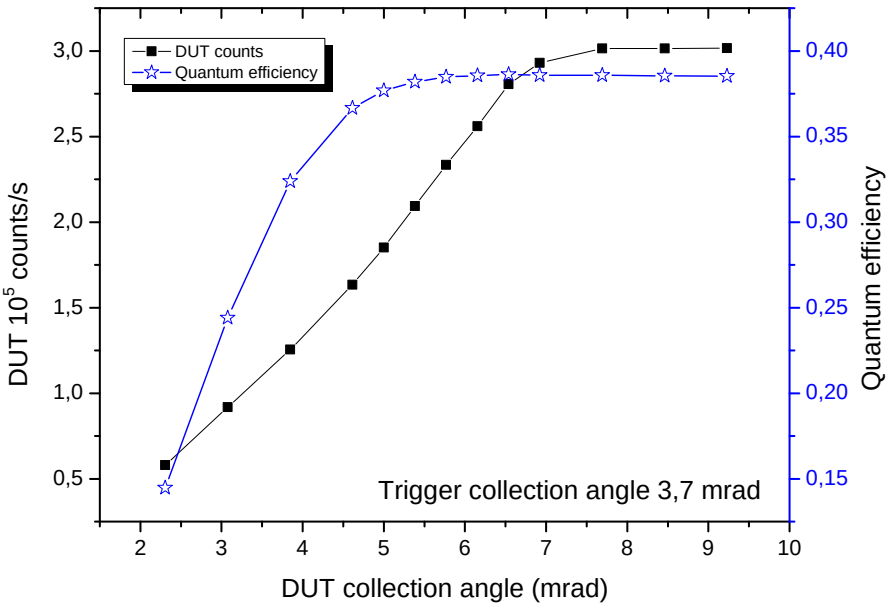

Figure 2.6: The quantum efficiency of the DUT (star) and its single count rate (square) are shown as the DUT collection iris is varied with the trigger detector collection angle of 3,7 mrad. Quantum efficiency is not corrected for crystal losses.

A check of the alignment of the DUT and trigger is obtained by scanning both detectors versus the collection angle to optimize the correlated signal. The collection angle is varied just by opening or closing the aperture mounted in front of each detector.

In Figure 2.6 a scan of quantum efficiency versus collection angle is presented. The quantum efficiency level out at a collection angle of about 6 mrad for a trigger collection angle of 3.7 mrad. The fact that the quantum efficiency reach the plateau before the DUT counts, evidence that the DUT detector collection angle include all the coincidence area. On the other hand, the DUT although reach a plateau, indicating that the cut off in the collected wavelengths is given by the interference filters and not by the spatial selection (iris).

2.3.3 True trigger rate determination

Since the method depends on trigger counts, indicating the existence of a correlated photon in the DUT channel, we must be able to accurately determine and remove spurious trigger count (not due to the PDC photons needed for our calibration scheme.)

While the evaluation of accidental coincidences is obtained by the measurement technique described in section 2.3, the average background counts $\langle m_B \rangle$ presented in equation 2.11 should be experimentally measured, because each detector is individually affected by background counts, resulting from stray light unrelated to the down-conversion pairs and electronic noise (dark counts and after pulses). The measurement of both dark counts and stray light together is performed using half-wave plate on the pump beam (see Figure 2.2). Such wave plate is used to rotate the polarization of the pump beam by $90\,^{\circ}$, which effectively turns off the creation of photon pairs, because the phase-matching constraints allow only one polarization orientation of the pump beam to produce down-converted light. The advantage of this scheme is that, while the production of photon pairs is stopped, all other contributions remain the same, allowing an excellent determination of the unwanted trigger counts.

2.3.4 Losses estimation

In order to obtain the efficiency of the DUT detector, the losses associated to the different optical components are measured. The transmittance of the interference filters and of the BBO crystal are measured with the Cary 5000 spectrophotometer facility (with 5 nm bandwith).

The interference filter on the trigger channel is centred around 651 nm, and full width at half maximum (FWHM) bandwidth of 3 nm and a maximum transmittance of approximately 69%. The interference filter on the DUT channel is centred around 763 nm with a FWHM bandwidth of 20 nm and a transmittance of approximately 65% at 761 nm.

The transmittance measurement of the BBO crystal is more tricky because polarized probe beam and sample tilting are required. A specially designed sample holder for the

spectrometer facility is used to hold a Glan-Taylor Calcite polarizer cube and a small goniometer, where the BBO crystal sits. The transmittance measurement of the BBO crystal is (81.50 ± 0.16) % at 761 nm. If the center of the crystal is considered as the mean point of down-conversion source, then the loss for the signal photon, to the exit of the crystal, is given by the square root of the crystal transmittance. As a result, the BBO's transmittance for PDC light generated at 761 nm is $\tau_{DUT} = (0.9028 \pm 0.0016)$.

2.4 Experimental results

The quantum efficiency measurements are performed at five different count rates, by attenuating the pump laser, ranging from 4×10^5 counts/s to a maximum of 4×10^6 counts/s. A large range of the safe working count rate of the SPAD ($< 10^7$ counts/s) is covered with this measurements. For each count rate, three consecutive measurements are performed: In the first the average coincidence counts $\langle m_c \rangle$, the mean valid start counts $\langle m_{vs}^{in} \rangle$ and mean DUT counts $\langle m_{DUT}^{meas} \rangle$ are registered. In the subsequent measurement, the coincidence peak is moved out of the coincidence windows by adding a delay in the DUT channel, and the valid start counts $\langle m_{vs}^{out} \rangle$ and the accidental coincidences $\langle A \rangle$ are collected. In the final step the half-wave plate is rotated to turn off the PDC light and the average background counts on valid start $\langle m_B \rangle$ are obtained. In each step and for each count rate, 96 measurements of 10 seconds each are recorded in order to have some statistics. The quantum efficiency η_{DUT} is calculated by means of Eq. (2.8) for each count rate.

By applying the uncertainty propagation law [50] to the model of Eq. (2.8), the statistical uncertainty associated with this two-photon measurement technique is deduced [44, 47, 48]:

$$\begin{aligned} u^2(\eta_{DUT}) = c_1^2 u^2(m_c) + c_2^2 u^2(A) + c_3^2 u^2(m_{vs}^{in}) + c_4^2 u^2(m_{vs}^{out}) + c_5^2 u^2(m_B) + \\ + c_6^2 u^2(\tau_{DUT}) + 2\rho_{1,3} c_1 c_3 \sqrt{u^2(m_c) u^2(m_{vs}^{in})} + 2\rho_{2,4} c_2 c_4 \sqrt{u^2(A) u^2(m_{vs}^{out})} \end{aligned} \tag{2.12}$$

were $u^2(x) = \langle x^2 \rangle - \langle x \rangle^2$ is the variance of a generic variable x. Sensitivity coefficients c_i are deduced by standard uncertainty propagation rules and the correlation coefficient $\rho_{i,j}$ are evaluated from repeated experimental data as $\rho_{i,j} = (\langle x_i x_j \rangle - \langle x_i \rangle \langle x_j \rangle)/\sqrt{u^2(x_i)u^2(x_j)}$.

As an example, the uncertainty budget for the quantum efficiency measurement at a DUT count rate of about 2 million counts/s is reported in Table 2.1. The standard uncertainty u_i is calculated as the square root of the variance, a cover factor $K = 1$ is used. The biggest source of uncertainty is given by the crystal's optical losses measurement, it is reasonable due to the difficult in the accuracy of tilting the crystal and polarizing the light.

The η_{DUT} is obtained for the five different count rates. On figure 2.7 it is shown the graph of η_{DUT} vs the DUT count rate where a lineal dependence can be observed. It is useful to observe the dependence of the DUT dead time with the amount of counts arriving to this detector: as higher the count rate, higher the dead time, and lower the quantum efficiency.

A regression analysis of the data is made using the least squares method $y = a + bx$ obtaining coefficients $a = (0,43555 \pm 6,5 \times 10^{-4})$ and $b = (-2,05 \times 10^{-8} \pm 2 \times 10^{-10})$, with a correlation coefficient of $R^2 = 0,9994$.

According with equation 2.10 the intercept $a = \eta_o$, is the efficiency of the detector in an ideal case of zero dead time. From the slope, the detector dead time is obtained as $t_D = -bT/\eta_0$, then $t_D = (47.1 \pm 0.5)ns$.

Table 2.1: Uncertainty budget for DUT calibration by two photon technique. The data corresponds to a set of 96 measurement of 10 seconds. $\langle m_{DUT}^{meas} \rangle = 20832830$ counts/s. The standard uncertainty is calculated with $K = 1$. G correspond to a Gaussian distribution while S correspond to a square one. The biggest contribution to the uncertainty is given by the optical losses in the crystal. The Quantum efficiency final uncertainty is about 0.1 %.

Quantity	Symbol	Value	Standard Uncertainty (u_i)	Distribution	Degree of freedom	Sensitivity coefficient (c_i)	Uncertainty contribution
Valid start counts with the peak	$\langle m_{vs}^{in} \rangle$	1992093	141	G	96	2.1×10^{-7}	3.0×10^{-5}
Valid start counts without the peak	$\langle m_{vs}^{out} \rangle$	2083865	167	G	96	9.2×10^{-9}	1.5×10^{-6}
Coincidence counts	$\langle m_c \rangle$	725735	90	G	96	5.6×10^{-7}	5.1×10^{-5}
Background counts	$\langle m_B \rangle$	39935	20	G	96	2.0×10^{-7}	4.0×10^{-6}
Accidental coincidences	$\langle A \rangle$	35544	19	G	96	5.4×10^{-7}	1.0×10^{-5}
Crystal optical losses	τ_{DUT}	0.9028	0.0016	S	∞	0.189	9.1×10^{-4}
Quantum efficiency	η_{DUT}	0.3925	0.0007				

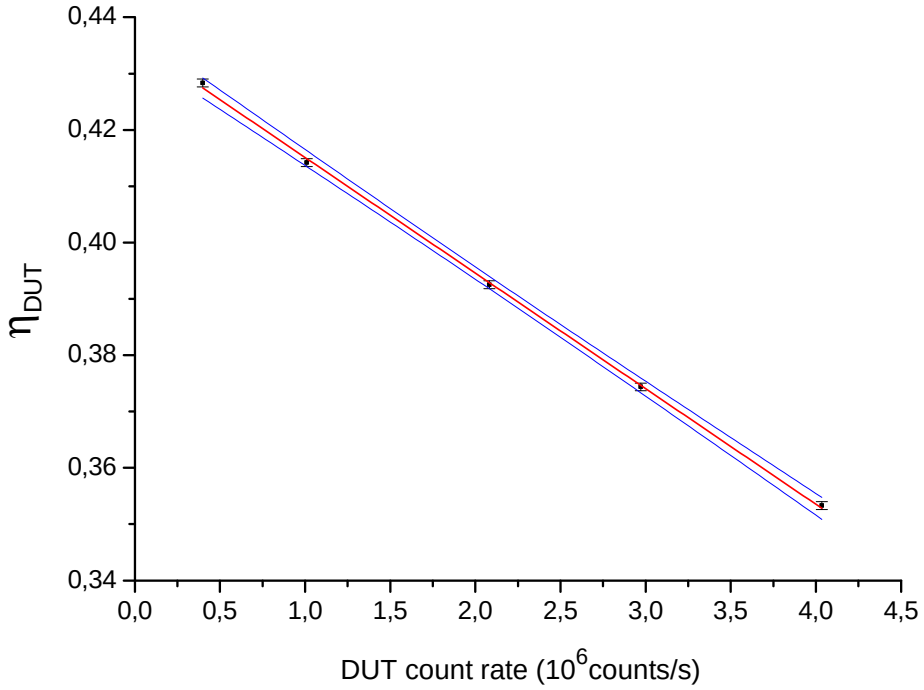

Figure 2.7: Graph of η_{DUT} vs the DUT count rate m_{DUT}^{meas} for five different count rate. Regression line (red) $y = a + bx$ with $a = (0,43555 \pm 6,5 \times 10^{-4})$ and $b = (-2,05 \times 10^{-8} \pm 2 \times 10^{-10})$. 95 % confidence bands are shown in blue.

2.5 Conventional substitution calibration

The main reason for single photon detector calibration using conventional calibration technique is to link the optical power level of 100 μW, typical of classical radiometry, down to few photon counting level, in order to hook single photon regime to SI (International System of Units). This calibration does not exploits quantum properties of twins correlated photons and was out of the goals of my PhD works; it is here summarized only for completeness. A successful linkage will also be a significant step in demonstrating the viability of redefining the candela in terms of a countable number of photons. This will provide the metrology techniques and validation across a broad spectrum of photon detection applications.

The conventional method is based on substitution calibration and the procedure is a direct comparison between the Single Photon Avalanche Detector (the DUT) and a Trap Transfer Detector (TTD) measuring the same laser beam. The measurement setup is schematically described in Figure 2.8. A TTD is a special geometrical arrangement of Silicon photodiodes, optically in series and electrically in parallel in order to add their currents [51], that is directly linked to an absolute standard, a cryogenic electrical substitution radiometer. To operate the DUT within its maximum safe count rate (10^7 counts/s) it is necessary to perform the comparison at very low power level, namely few picowatt. For the TTD, the measurement at such low power level, with an uncertainty comparable with the state of the art [52], is an highly demanding task requiring trap detectors with low dark-current, very sensitive current measurement electronics, and a stabilized and strongly attenuated laser source that preserves beam shape and long-term stability.

The readout of the two detectors, placed alternatively into the same laser beam of power flux Φ are given by the following equations

$$\begin{aligned} V &= \eta_{TTD}\ e\ \tfrac{\Phi}{h\nu}\ R \\ C &= \eta_{DUT}\tfrac{\Phi}{h\nu} \end{aligned} \tag{2.13}$$

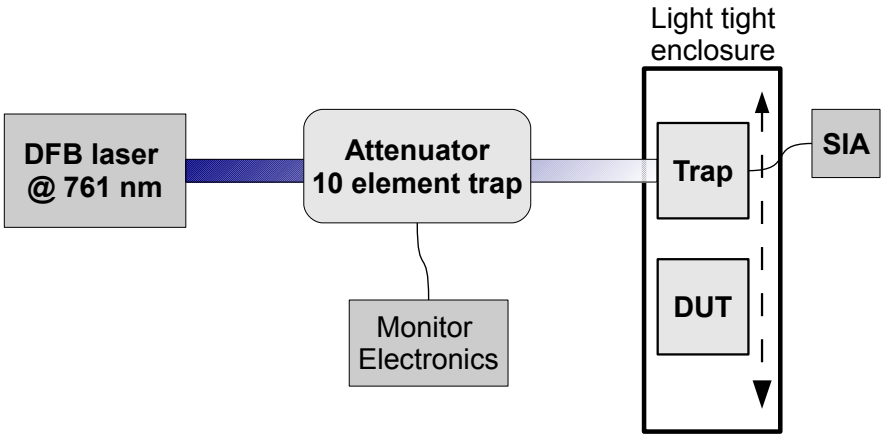

Figure 2.8: Scheme of the setup used in the substitutional calibration method. The source was a distributed feedback laser (DFB) diode power stabilized with a feedback system. The high power delivered from the source system is attenuated by means of a ten element trap detector retaining the quality of the incoming beam [53]. The Trap transfer standard and the DUT are mounted on a linear translation stage allowing their alternate alignment on the beam at the output of the attenuator. The faint photocurrent output from the Trap transfer standard is converted into a voltage by means of a low-noise Switching Integrating Amplifier (SIA).

where V is the output voltage from the Switched Integrator Amplifier (SIA) of the Trap transfer standard, R is the gain of the SIA, C is the mean count rate of the DUT, η_{TTD} is the quantum efficiency of the trap transfer standard detector, η_{DUT} is the quantum efficiency of the DUT, e is the electron charge, h is the Planck constant and ν is the laser frequency. The quantum efficiency of DUT is hence

$$\eta_{DUT} = \eta_{TTD}\ e\ R\ \frac{C - C_o}{V - V_o} \tag{2.14}$$

were C_o and V_o are the background readouts (without laser light) of the trap transfer standard (after SIA) and of the DUT, respectively.

With the aim to have an independent measurement, the DUT detector was sent to the Physikalisch-Technische Bundesanstalt laboratories (PTB) in Germany in order to carry out the classical calibration. Measurements were performed at relatively large count rate for SPAD, at about 4 million counts/s and 1 million counts/s (i.e. an optical power flux of about 2 pW and 380 fW, respectively).

Chapter 3

Quantum measurements

3.1 Quantum operations

The quantum operations formalism is a general tool for describing the evolution of quantum systems in a wide variety of circumstances. A quantum system can be described through its density operator (or density matrix) ρ, defined as:

$$\rho \equiv \sum_i p_i \left|\psi_i\right\rangle \left\langle\psi_i\right| \tag{3.1}$$

with $p_i \geq 0$ and $\sum_i P_i = 1$. For a single stage process, the output state ρ' is related to the input state ρ by the equation

$$\rho' = \mathcal{E}(\rho). \tag{3.2}$$

The map $\mathcal{E}$ in this equation is a quantum operation, describing the dynamic change to a state which occurs as the result of some physical process. By applying an unitary evolution operator U as a quantum operation, we may write $\rho \to \mathcal{E}(\rho) \equiv U\rho U^\dagger$.

The dynamics of a closed quantum system are described by unitary transformations. A natural way to describe the dynamics of an open quantum system is to regard it as arising from an interaction between the system of interest, which we shall call the principal system, and the environment, which together form a closed quantum system.

In other words, suppose we have a system in state ρ, which is sent into a box which is coupled to an environment. In general the final state of the system, $\mathcal{E}(\rho)$, may not be related by a unitary transformation to the initial state ρ. We assume (for now) that the system-environment input state is a product state, $\rho \otimes \rho_{env}$. After the box's transformation U the system no longer interacts with the environment, and thus we perform a partial trace over the environment to obtain the reduced state of the system alone:

$$\mathcal{E}(\rho) = tr_{env}\left[U\left(\rho \otimes \rho_{env}\right)U^{\dagger}\right]. \tag{3.3}$$

Quantum operations can be represented in an elegant form known as the operator-sum representation. Let $|e_n\rangle$ be an orthonormal basis for the (finite dimensional) state space of the environment, and let $\rho_{env} = |e_0\rangle\langle e_0|$ be the initial state of the environment. There is no loss of generality in assuming that the environment starts in a pure state [54]. Although this extra system is 'fictitious', it makes no difference to the dynamics experienced by the principal system. Then, for a system in a initial state ρ, the final state can be written as:

$$\begin{aligned} \mathcal{E}(\rho) &= \sum_n \langle e_n| U[\rho \otimes |e_0\rangle\langle e_0|]U^{\dagger}|e_n\rangle & (3.4)\\ &= \sum_n K_{(n)}\rho K_{(n)}^{\dagger} & (3.5) \end{aligned}$$

where $K_{(n)} \equiv \langle e_n| U |e_0\rangle$ is an operator on the state space of the principal system. Equation (3.5) is known as the operator-sum representation of $\mathcal{E}$. The operators $\{K_{(n)}\}$ are known as operation elements for the quantum operation $\mathcal{E}$.

The operation elements satisfy an important constraint known as the completeness relation. In the classical case, the completeness relation arose from the requirement that probability distributions be normalized to one. In the quantum case the completeness

relation arises from the analogous requirement that the trace of $\mathcal{E}(\rho)$ be equal to one,

$$\begin{aligned} 1 &= tr\left(\mathcal{E}(\rho)\right) && (3.6)\\ &= tr\left(\sum_n K_{(n)}\rho K_{(n)}^\dagger\right) && (3.7)\\ &= tr\left(\sum_n K_{(n)}^\dagger K_{(n)}\rho\right) && (3.8)\end{aligned}$$

Since this relationship is true for all ρ it follows that we must have

$$\sum_n K_{(n)}^\dagger K_{(n)} = I \tag{3.9}$$

This equation is satisfied by quantum operations which are trace-preserving.

For non-trace-preserving quantum operations, for which $\sum_n K_{(n)}^\dagger K_{(n)} \leq I$, the transformation (3.5) occurs with generally non-unit probability $tr[\mathcal{E}(\rho)] \leq 1$ [55]. The particular case of unitary transformations corresponds to having only one term $K_{(n)} = U$ in the sum (3.5), with U unitary. However, we can consider also nonunitary operations with only one term, i.e.,

$$\mathcal{E}(\rho) = A\rho A^\dagger, \tag{3.10}$$

being A a contraction, i.e., $\parallel A \parallel \leq 1$: this last operations are called *pure*, since they leave pure states ρ as pure. Indeed, for $\rho = |\varphi\rangle\langle\varphi|$ we can write the transformation $\rho \to \frac{\mathcal{E}(\rho)}{tr(\mathcal{E}(\rho))}$ as:

$$|\varphi\rangle \to \frac{A|\varphi\rangle}{\parallel A|\varphi\rangle \parallel}. \tag{3.11}$$

There is a nice interpretation that can be given to the operator-sum representation. Imagine that a measurement of the environment is performed in the basis $|e_0\rangle$ after the unitary transformation U has been applied. Applying the principle of implicit measurement [54], we see that such a measurement affects only the state of the environment, and does not change the state of the principal system. Let ρ_n be the state of the principal

system given that outcome n occurs,

$$\rho_n \propto tr_E(|e_n\rangle\langle e_n| U(\rho \otimes |e_0\rangle\langle e_0|)U^\dagger |e_n\rangle\langle e_n|) = \langle e_n| U(\rho \otimes |e_0\rangle\langle e_0|)U^\dagger |e_n\rangle \quad (3.12)$$

$$= K_{(n)}\rho K_{(n)}^\dagger. \quad (3.13)$$

Normalizing ρ_n

$$\rho_n = \frac{K_{(n)}\rho K_{(n)}^\dagger}{tr(K_{(n)}\rho K_{(n)}^\dagger)} \quad (3.14)$$

we find the probability of outcome k is given by

$$p(n) = tr\left(|e_n\rangle\right)\langle e_n| U(\rho \otimes |e_0\rangle\langle e_0|)U^\dagger |e_n\rangle\langle e_n| \quad (3.15)$$

$$= tr(K_{(n)}\rho K_{(n)}^\dagger). \quad (3.16)$$

Thus

$$\mathcal{E}(\rho) = \sum_n K_{(n)}\rho K_{(n)}^\dagger = \sum_n p(n)\rho_n. \quad (3.17)$$

This gives us a beautiful physical interpretation of what is going on in a quantum operation with operation elements $\{K_{(n)}\}$. The action of the quantum operation is equivalent to taking the state ρ and randomly replacing it by $K_{(n)}\rho K_{(n)}^\dagger / tr(K_{(n)}\rho K_{(n)}^\dagger)$, with probability $tr(K_{(n)}\rho K_{(n)}^\dagger)$. In this sense, it is very similar to the concept of noisy communication channels used in classical information theory.

3.2 Matrix elements of an arbitrary quantum operation

In this section, we will focus in the formalism to determine experimentally an unknown quantum operation $\mathcal{E}$. The method analysed exploits the quantum parallelism of entanglement [56] to run all possible input states in parallel using only a single entangled state as the input in a tomographic reconstruction. This is a general method for experimentally determining the quantum operation matrix, using any available quantum-tomographic

scheme for the system in consideration, and a single fixed entangled state at the input.

Let us consider, for simplicity, a pure quantum operation in the form (3.11). We want to determine experimentally the matrix $A = \{A_{ij}\}$, with $A_{ij} = \langle i| A |j\rangle$, given an orthonormal basis $\{|j\rangle\}$ corresponding to some physical observable. Instead of acting with the contraction A on an "isolated" system, we perform the map on a system which is entangled in the state $|\psi\rangle\rangle = \sum_{mn} \psi_{mn}|m\rangle_A \otimes |n\rangle_B$. By applying the operator $\hat{A} = \sum_{ik} A_{ik}|i\rangle\langle k|$ to the state $|\psi\rangle\rangle$, we obtain

$$
\begin{aligned}
(\hat{A} \otimes I)|\psi\rangle\rangle &= \sum_{ikj} A_{ik}|i\rangle_A\langle k|_A \otimes |j\rangle_B\langle j|_B \sum_{mn} \psi_{mn}|m\rangle_A \otimes |n\rangle_B && (3.18)\\
&= \sum_{ikj} A_{ik}\psi_{kj}|i\rangle_A \otimes |j\rangle_B && (3.19)
\end{aligned}
$$

and

$$
\begin{aligned}
||A\psi||^2 &= ((\hat{A} \otimes I)|\psi\rangle\rangle)^\dagger((\hat{A} \otimes I)|\psi\rangle\rangle) && (3.20)\\
&= \sum_{ikj}\sum_{mnp} A_{ik}\psi_{kj}A^*_{mn}\psi^*_{np}\langle m|i\rangle_A\langle p|j\rangle_B && (3.21)\\
&= \sum_{ikjn} A_{ik}\psi_{kj}A^*_{in}\psi^*_{nj} && (3.22)
\end{aligned}
$$

Then, the transformation is:

$$
\begin{aligned}
|\psi\rangle\rangle \to |\phi\rangle\rangle &= \frac{(\hat{A} \otimes I)|\psi\rangle\rangle}{||A\psi||} && (3.23)\\
&= \sum_{ij} \phi_{ij}|i\rangle_A \otimes |j\rangle_B && (3.24)
\end{aligned}
$$

with

$$
\phi_{ij} = \frac{A_{ik}\psi_{kj}}{||A\psi||} \tag{3.25}
$$

then, the elements of the quantum operator matrix, in terms of the input and output

state matrices is written as:

$$||A\psi||\phi_{ij}\psi^{-1}_{jl} = A_{ik}\cancelto{\delta_{kl}}{\psi_{kj}\psi^{-1}_{jl}} = A_{il} \tag{3.26}$$

where the entanglement state is assumed to have invertible matrix ψ.

In this formalism, the matrix ϕ corresponding to the output state can be written in terms of measurable ensemble averages as follows

$$\phi_{ij} = \langle\langle i,j|\phi\rangle\rangle = e^{i\theta}\frac{\langle|i_0,j_0\rangle\rangle\langle\langle i,j|\rangle}{\sqrt{\langle|i_0,j_0\rangle\rangle\langle\langle i_0,j_0|\rangle}} = e^{i\theta}\frac{\phi^*_{i_0j_0}\phi_{ij}}{\sqrt{|\phi_{i_0j_0}|^2}} \tag{3.27}$$

where the ensemble at the output is denoted by $\langle ...\rangle \equiv \langle\langle\phi|...|\phi\rangle\rangle$, $|i,j\rangle\rangle \equiv |i\rangle \otimes |j\rangle$, i_0, j_0 are suitable fixed integers, and $e^{i\theta}$ is an irrelevant overall phase factor corresponding to $\theta = arg(\langle\langle i,j|\phi\rangle\rangle)$. To rewrite the matrix A_{ij} in terms of the output ensemble averages, we define the operator

$$E_{ij}(\psi) = |i_0\rangle\langle i| \otimes |j_0\rangle\langle(\psi^{-1})^*(j)| \tag{3.28}$$

where

$$\langle(\psi^{-1})^*(j)| = \sum_l (\psi^{-1}_{lj})^*\langle l|. \tag{3.29}$$

The matrix elements A_{ij} in terms of the introduced operator can be written as

$$A_{ij} = k\langle E_{ij}(\psi)\rangle \tag{3.30}$$

with

$$k = e^{i\theta}\sqrt{\frac{||A\psi||^2}{|\phi_{i_0j_0}|^2}} \tag{3.31}$$

It is easy to prove that expression (3.30) is equivalent to (3.26).

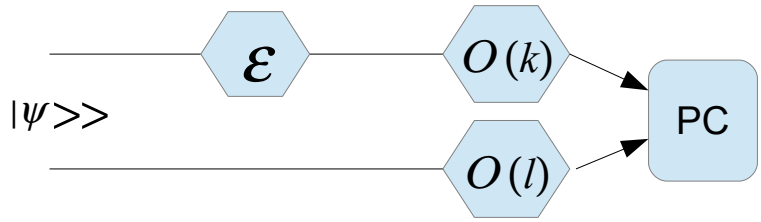

Figure 3.1: General scheme for the experiment for the tomographic estimation of a quantum operation. $|\psi\rangle\rangle$ is an entangled state prepared with two identical quantum systems. In one of the systems the quantum operation $\mathcal{E}$ is applied, while the other system is left undisturbed. At the output, quantum tomographic estimations are made by measuring jointly two random observables from a quorum $\{O(l)\}$.

Written as (3.30), A_{ij} can be estimated using quantum tomography [54,57]: a method to estimate the ensemble average $\langle H\rangle$ of any arbitrary operator H by using only measurement outcomes of a quorum of observables $\{O(l)\}$ [58], with orthonormal resolution, sufficient to give a complete quantum information of the system. The operator H can be expanded as $H = \sum_l tr\left[Q^\dagger(l)H\right] O(l)$, where $Q(l)$ and $O(l)$ form a bi-orthogonal set such that $tr\left[Q^\dagger(i)O(j)\right] = \delta_{ij}$. Therefore, the tomographic estimation of the ensemble average $\langle H\rangle$ is obtained as the double average (over the ensemble and the quorum), of the unbiased estimator $tr\left[Q^\dagger(l)H\right] O(l)$ with a random l. For multipartite quantum systems, the quorum can be the tensor product of single system quorums [59]: this means, that is just necessary to make two local quorum measurement jointly on the two systems and analyze data with tensor product estimators.

A general scheme for the experiment of the tomographic estimation of a quantum operation matrix applying this method, is shown in Figure 3.1.

The method described above can be easily generalized to the case of arbitrary non-pure quantum operations. The output state in this case is the density matrix

$$|\psi\rangle\rangle\langle\langle\psi| \to R(\psi) = \mathcal{E} \otimes I(|\psi\rangle\rangle\langle\langle\psi|) \tag{3.32}$$

Using $|\psi\rangle\rangle = \sum_{lm} \psi_{lm}|l\rangle \otimes |m\rangle$ and the quantum operation $\mathcal{E}(\rho) = \sum_{(n)} \hat{K}_{(n)}\rho\hat{K}^\dagger_{(n)}$ in Eq. (3.32), where $\hat{K}_{(n)} = \sum_{ij} K_{(n)ij}|i\rangle\langle j|$, it is possible to rewrite the final state $R(\psi)$

as

$$R(\psi) = \sum_{(n)} K_{(n)} \otimes I|\psi\rangle\rangle\langle\langle\psi|K_{(n)}^{\dagger} \otimes I \tag{3.33}$$

$$= \sum_{(n)} \sum_{kji'j'k'} K_{(n)ij}\psi_{jk}K^{*}_{(n)i'j'}\psi^{*}_{j'k'}|i\rangle\langle i'| \otimes |k\rangle\langle k'| \tag{3.34}$$

The quantum operation can be written in terms of the density matrix $R(\psi)$, for ψ equal to the identity matrix I, as

$$\mathcal{E}(\rho) = tr_2\left[I \otimes \rho^T R(I)\right] \tag{3.35}$$

where tr_2 is the partial trace on the second Hilbert space. In the follow it will be shown the validity of Eq. (3.35). The expansion of the left side of the equation is

$$\mathcal{E}(\rho) = \sum_{(n)} \hat{K}_{(n)}\rho\hat{K}^{\dagger}_{(n)} \tag{3.36}$$

$$= \sum_{(n)} \sum_{iji'j'} \sum_{mp} K_{(n)ij}\rho_{mp}K^{*}_{(n)i'j'}|i\rangle\langle j|m\rangle\langle p|j'\rangle\langle i'| \quad (\delta_{jm},\ \delta_{pj'}) \tag{3.37}$$

$$= \sum_{(n)} \sum_{iji'j'} K_{(n)ij}\rho_{jj'}K^{*}_{(n)i'j'}|i\rangle\langle i'| \tag{3.38}$$

Then, for the right term of Eq. (3.35), we have

$$\left(I \otimes \hat{\rho}^T\right) R(I) = \left(\sum_{lpm} \rho_{pm}|l\rangle\langle l| \otimes |m\rangle\langle p|\right) \sum_{(n)iji'j'} k_{(n)ij}k^{*}_{(n)i'j'}|i\rangle\langle i'| \otimes |j\rangle\langle j'| \tag{3.39}$$

$$= \sum_{m(n)} \sum_{iji'j'} k_{(n)ij}\rho_{jm}k^{*}_{(n)i'j'}|i\rangle\langle i'| \otimes |m\rangle\langle j'| \tag{3.40}$$

applying the trace in the second system of Eq. (3.40) it is easy to arrive to Eq. (3.38), and in this way the validity of Eq. (3.35) is shown.

For invertible ψ the two matrices $R(I)$ and $R(\psi)$ are connected by

$$R(I) = (I \otimes (\psi^{-1})^T)R(\psi)(I \otimes (\psi^{-1})^*). \tag{3.41}$$

Therefore, it is possible to obtain the matrix R in Eq. (3.35), which is in one-to-one correspondence with the quantum operation $\mathcal{E}$, by estimating via quantum tomography, the output ensemble averages:

$$\langle\langle i,j\,|R(I)|\,l,k\rangle\rangle = \langle E_{lk}(\psi)E_{i,j}(\psi)\rangle \tag{3.42}$$

$$= \left\langle |l\rangle\langle i| \otimes \left|(\psi^{-1})^*(k)\right\rangle \left\langle (\psi^{-1})^*(j)\right|\right\rangle . \tag{3.43}$$

3.3 Positive operator valued measure

For some applications, the post-measurement state of the system is of little interest, with respect to the measurement outcomes. In such cases there is a mathematical tool known as Positive Operator-Valued Measure (POVM) which is especially well adapted to the analysis of the measurements [54].

Suppose a measurement (described by *measurement operators* M_n) is performed to a quantum system in the state $|\psi\rangle$: the probability of outcome n is given by $p(n) = \langle\psi| M_n^\dagger M_n |\psi\rangle$. Suppose we define

$$\Pi_n \equiv M_n^\dagger M_n \tag{3.44}$$

Π_n is a positive operator such that $\sum_n \Pi_n = I$ and $p(n) = \langle\psi|\,\Pi_n\,|\psi\rangle$. Thus the set of operators Π_n are sufficient to determine the probabilities of the different measurement outcomes. The operators Π_n are known as the POVM *elements* associated with the measurement. The complete set $\{\Pi_n\}$ is known as a POVM.

Projective measurements described by projectors P_n, such that $P_n P_n' = \delta_{n,n'} P_n$ and $\sum_n P_n = I$, are an interesting example of POVM. In this case, all the POVM elements are the same as the measurement operators themselves, since $\Pi_n \equiv P_n^\dagger P_n = P_n$.

In the following, it will be shown that if $\{\Pi_n\}$ is some arbitrary set of positive operators such that $\sum_n \Pi_n = I$, there exists a set of measurement operators M_n defining the measurement described by the POVM $\{\Pi_n\}$.

Defining $M_n \equiv \sqrt{\Pi_n}$ we see that $\sum_n M_n^\dagger M_n = \sum_n \Pi_n = I$, and therefore the set

$\{M_n\}$ describes a measurement with POVM $\{\Pi_n\}$.

It is convenient to define a POVM to be any set of operators $\{\Pi_n\}$ such that: (a) each operator Π_n is positive; and (b) the completeness relation $\sum_n \Pi_n = I$ is satisfied, expressing the fact that probabilities sum to one. We note again that, given a POVM $\{\Pi_n\}$, the probability of outcome n when a quantum system in the state $|\psi\rangle$ is measured, is given by $p(n) = \langle\psi| \Pi_n |\psi\rangle$.

In the density matrix formalism, given an input state ρ, the probability $p(n)$ of obtaining output n is given by [60]

$$p(n, \rho) = tr[\rho \Pi_n]. \tag{3.45}$$

Chapter 4

Quantum characterization of superconducting photon counters

The possibility of discriminating the number of impinging photons on a detector is a fundamental tool in many different fields of optical science and technology. At the moment, the most promising genuine PNR detectors are visible light photon counters [61] and transition edge sensors (TESs) [62–64], i.e. micro calorimeters based on a superconducting thin film working as a very sensitive thermometer. For the practical application of these detectors, it is crucial to achieve their precise characterization [65]. In particular, it is generally assumed that TESs are linear photon counters, with a detection process corresponding to a binomial convolution. It is also expected that dark counts are not present in TESs. A tomography of the POVM elements of the TES provides the full characterization of the detector at the quantum level. In this chapter we present a full tomography of the TES POVM, exploiting an effective and statistically reliable technique based on recording the detector response for an ensemble of coherent signals providing a sample of the Q-function of the POVM [64].

4.1 Tomography of quantum detectors

To fully characterize a quantum detector, data obtained from measuring input states from a well-known source is needed.

From the measured statistics $p(n, j)$ (where $p(n, j)$ is the probability of obtaining an output n given an input state ρ_j), all the POVM elements $\{\Pi_n\}$ can be recovered if probe states or input states are chosen to form a set $\{\rho_j\}$ that is tomographically complete: the span of the operators $\{\rho_j\}$ (which are not necessarily linearly independent) must cover the entire Hilbert space to which the POVM elements belong [60].

Coherent states $|\alpha\rangle$ are ideal candidates in the case of PNR detectors, since a laser can generate them directly and we can create a tomographically complete set of probe states $\{|\alpha\rangle \langle\alpha|\}$ by transforming their amplitude $|\alpha|$ and their phase $\arg(\alpha)$.

Notably, a full representation of the detector is given by the measured statistics, when coherent states are used as probes. If we consider a set of K coherent states of different amplitudes $|\alpha_j\rangle$, $j = 1, \ldots, K$, it is possible to reconstruct the Q-function of the detector, which is simply proportional to the measured statistics [60],

$$p(n, j) = \frac{1}{\pi^2} \langle\alpha_j| \Pi_n |\alpha_j\rangle = \frac{1}{\pi} Q_n(j) \tag{4.1}$$

Since $Q_n(j)$ of each POVM contains the same information as the element Π_n itself, predictions of the detection probabilities for arbitrary input states can then be calculated directly from the Q-function.

The POVM elements of a phase insensitive PNR detector are diagonal operators in the Fock basis, i.e. $\Pi_n = \sum_m \Pi_{nm} |m\rangle \langle m|$, with completeness relation $\sum_n \Pi_n = I$. The matrix elements $\Pi_{nm} = \langle m| \Pi_n |m\rangle$ describe the detector response to m incoming photons, i.e. the probability of detecting n photons with m photons at the input. Using coherent states the probability of detecting n photons (of obtaining the outcome n), with the j^{th} state as input is given by:

$$p(n,j) = tr\left[\left|\alpha_j\right\rangle \left\langle\alpha_j\right| \Pi_n\right] = \sum_m \Pi_{nm} q_{mj} \tag{4.2}$$

where

$$q_{mj} = e^{-\mu_j} \frac{\mu_j^m}{m!} \tag{4.3}$$

is the ideal photon statistics of the coherent state $|\alpha_j\rangle$, and $\mu_j = |\alpha|^2$ is its average number of photons [41]. For a perfect photon-number-resolving detector that can discriminate up to eight photons, the outcome probability distributions would be the one shown in Figure 4.1.

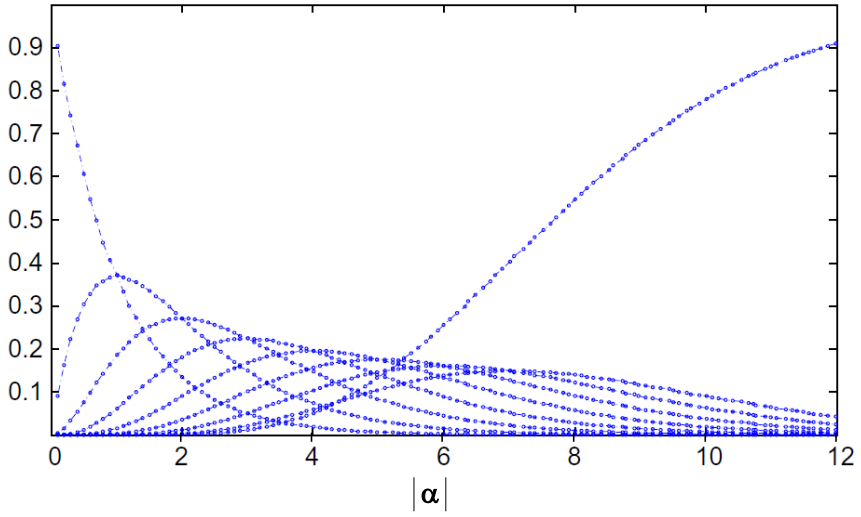

Figure 4.1: Outcome probability distributions for a nine-outcome detector. Each curve represents the probability of that outcome (0 clicks, 1 click, ..., 9 clicks) happening versus the value of the intensity of the coherent state arriving at the detector. This graph was taken from reference [60].

The probabilities $p(n,j)$ are sampled and the statistical model composed by the set of Eq. (4.2) is inverted in order to reconstruct the POVM matrix elements, Π_{nm}. Since the Fock space is infinite dimensional, this estimation problem contains, in principle, an infinite number of unknowns. However, given the set of probing coherent states, we can find a Fock number M for which we have a small number of data for the entries with $m > M$ and we cannot investigate the performances of the detector above the corresponding

energy regimes. In consequence, a suitable truncation at a certain dimension M should be performed, with the constraint that the probability of having $m > M$ photons in the states $|\alpha_j\rangle$ is small enough. The constrain ensures that the truncation of the Hilbert space does not cause any loss of information. The above argument also makes clear that a little extra care should be taken for the entries just below this regime, i.e. Π_{nm} with m just below M. In fact, for this entries, the estimation problem is generally ill-conditioned, i.e. small fluctuation in the measured $p(n, j)$ may lead to large fluctuations in the reconstruction. Note that, according with Eq. (4.2), the Π_{nm} with m close to M have small weights q_{mj} and therefore the $p(n, j)$ are almost insensitive to their values.

As mentioned before, a sample of the Q-functions of the POVM elements are provided by the distributions $p(n, j)$ in Eq. (4.2). Any reconstruction scheme for the Π_{nm} basically amounts to recovering the Fock representation of the Π_n's from their phase space Q-representation. In general, this cannot be done exactly due to singularity of the antinormal ordering of the Fock number projectors $|n\rangle\langle n|$ [66]. On the other hand, upon exploiting the truncation described above, we deal with POVM elements expressed as a finite mixture of Fock states, which are amenable to reconstruction [67, 68]. Maximum likelihood (ML) methods or a suitable approximation of ML should be used to solve the statistical model in Eq. (4.2). We found that reliable results are obtained already with a least-squares fit, i.e. we have effectively estimated Π_{nm} by the minimization of a regularized version of the square difference

$$\sum_{n,j} \left(\sum_{m=0}^{M-1} q_{mj} \Pi_{nm} - p(n, j) \right)^2 \tag{4.4}$$

where the physical constraint of smoothness is implemented by exploiting a convex, quadratic and device-independent function [69]. The normalization constrain is also used, $\sum_{n=0}^{N-1} \Pi_{nm} = 1$, $\forall m$, where the last POVM element is defined as $\Pi_{N-1} = 1 - \sum_{n=0}^{N-2} \Pi_n$.

4.2 POVM reconstruction of a transition edge sensor

In this section, an experiment to reconstruct the POVM elements of TES is presented. An article based on this experiment was published in the New Journal of Physics, reference [64]

4.2.1 Experimental setup

The experimental setup used in this experiment is shown in Figure 4.2. A power stabilized fiber-coupled pulsed laser at 1570 nm with a pulse width of 37 ns and repetition rate of 9 kHz is used to illuminate the TES. The laser pulse is also used to trigger the data acquisition for a temporal window of 100 ns. A calibrated power meter is used to measure the laser pulse energy (365 ± 2) pJ. Two fiber-coupled calibrated attenuators in cascade are used to attenuate the laser to the photon-counting regime. A single-mode optical fiber is used to send the attenuated laser pulses to the TES. The set of coherent states needed to perform the POVM reconstruction has been generated by lowering the primary laser pulse energy from an initial attenuation of 63,5 dB to 76,5 dB (corresponding to an average of 130 and 6,5 photon per pulse respectively), to obtain 20 different states $|\alpha_j\rangle = \left|\sqrt{\tau_j}\alpha\right\rangle$, with $j = 1, ..., 20$ and where τ_j is the channel transmissivity.

The TES characterized in this experiment is composed of a $\sim$90 nm thick Ti/Au film [70, 71], fabricated by e-beam deposition on silicon nitride substrates. The effective sensitive area, obtained by lithography and chemical etching, is $20 \times 20\ \mu m^2$. The superconducting wirings of Al, with thicknesses between 100 and 150 nm, have been defined by a lift-off technique combined with radiofrequency sputtering of the superconducting films. Upon varying the top Ti film thickness, the critical temperatures of these TESs can range between 90 and 130 mK, showing a sharp transition (1–2 mK).

The characterization of TES has been carried out in a dilution refrigerator with a base temperature of 30 mK. Furthermore, the detector is voltage biased, in order to take advantage of the negative electro-thermal feedback, providing the possibility of obtaining a self-regulation of the bias point without a fine temperature control and reducing the

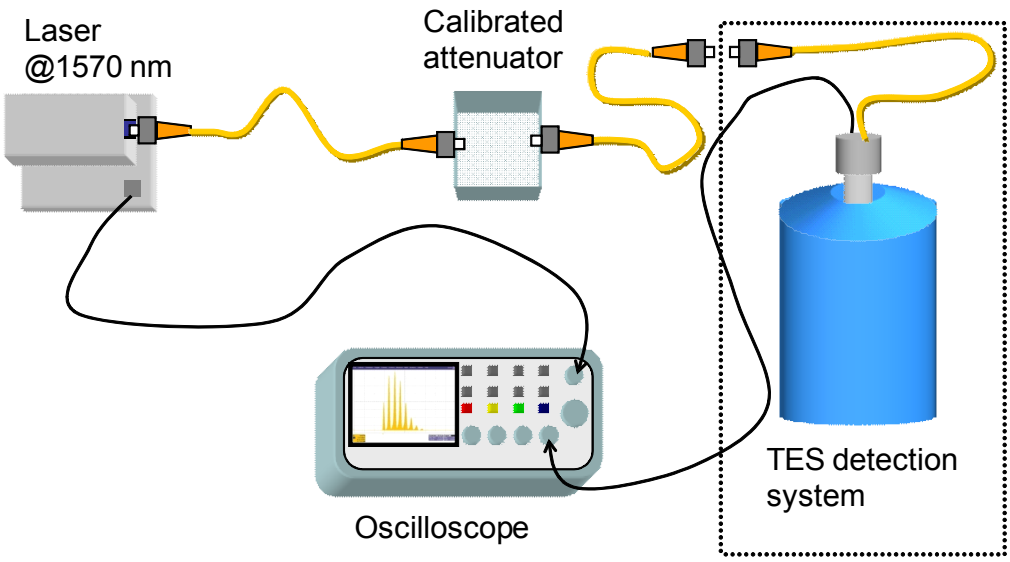

Figure 4.2: Experimental setup for the reconstruction of the POVM elements of a TES detector. A fiber coupled calibrated attenuator is used to attenuate a frequency stabilized pulsed laser at 1570 nm and generate 20 different states. The attenuated pulses are sent to the TES detection system using a single-mode optical fiber. The read-out operations are performed with a DC-SQUID current sensor, using electronics at room temperature. The SQUID output is addressed to an oscilloscope triggered by the laser. Data acquisition, first elaboration and storage are performed by the oscilloscope.

detector response time.

A DC-SQUID current sensor [72] is used for read-out operations on our TES, associated with room-temperature SQUID electronics. Finally, the SQUID output is addressed to a LeCroy 400 MHz oscilloscope, performing the data acquisition, first elaboration and storage.

4.2.2 Results

In the experiment, a fixed wavelength $\lambda = 1570$ nm is used thus, in ideal conditions, a discrete energy distribution with outcomes separated by a minimum energy gap $\Delta E = hc/\lambda$ is expected. Experimentally, a distribution with several peaks is observed, whose FWHM is determined by the energetic resolution of the whole TES detection device.

In a first calibration run, the experimental data is fitted with a sum of independent

Gaussian functions. The fit for nine data sets corresponding to nine different coherent states $|\alpha_j\rangle$ are shown in the left plots of Figures 4.3, 4.4 and 4.5. In these graphs, each point corresponds to a binning of an amplitude interval of 1,3 mV. An excellent agreement between data and the functions is observed. The '0-peak', corresponding to no photon detection, is the first peak on the left. The local minima of the fits, allow us to fix the amplitude thresholds corresponding to n detected photons. The counts in the intervals identified by these thresholds are summed and the histogram of counts is obtained. To evaluate the distributions $p(n, j)$ the histogram bars are normalized to the total number of events for the given state $|\alpha_j\rangle$. Some bias or fluctuations may be introduced by this threshold-based counts binning, since the tails of the n^{th} Gaussian peak fall out of the n counts interval. On the other hand, the effects in neighboring peaks compensate for each other and, overall, do not affect the tomographic reconstruction. In the histograms on the right of Figures 4.3, 4.4 and 4.5, the experimental probability distributions $p(n, j)$ are compared with the corresponding Poisson distributions of mean value $\eta\mu$ (with $\eta = 6,70\%$), for each of the nine states shown. As evident from the plots, the experimental results are in remarkable agreement with the theoretical predictions, showing a fidelity above of $99,5\%$, as reported in Figure 4.6.

The POVM reconstruction of our TES detection system has been performed up to $M = 140$ incoming photons and considering $N = 12$ POVM elements Π_n, $n = 0, ..., 11$. The probability operator of detecting more than 10 photons is given by $\Pi_{11} = 1 - \sum_{n=0}^{10} \Pi_n$.

The matrix elements Π_{nm} of the POVM operators for $0 \leq m \leq 100$ incoming photons, are shown in Figure 4.7. The reconstructed Π_{nm} are represented by bars, while the solid lines denote the matrix elements of a linear detector. In fact, the POVM of a linear photon counter takes the form of a binomial distribution

$$\Pi_n = \sum_{m=n}^{\infty} B_{nm} |m\rangle\langle m| \tag{4.5}$$

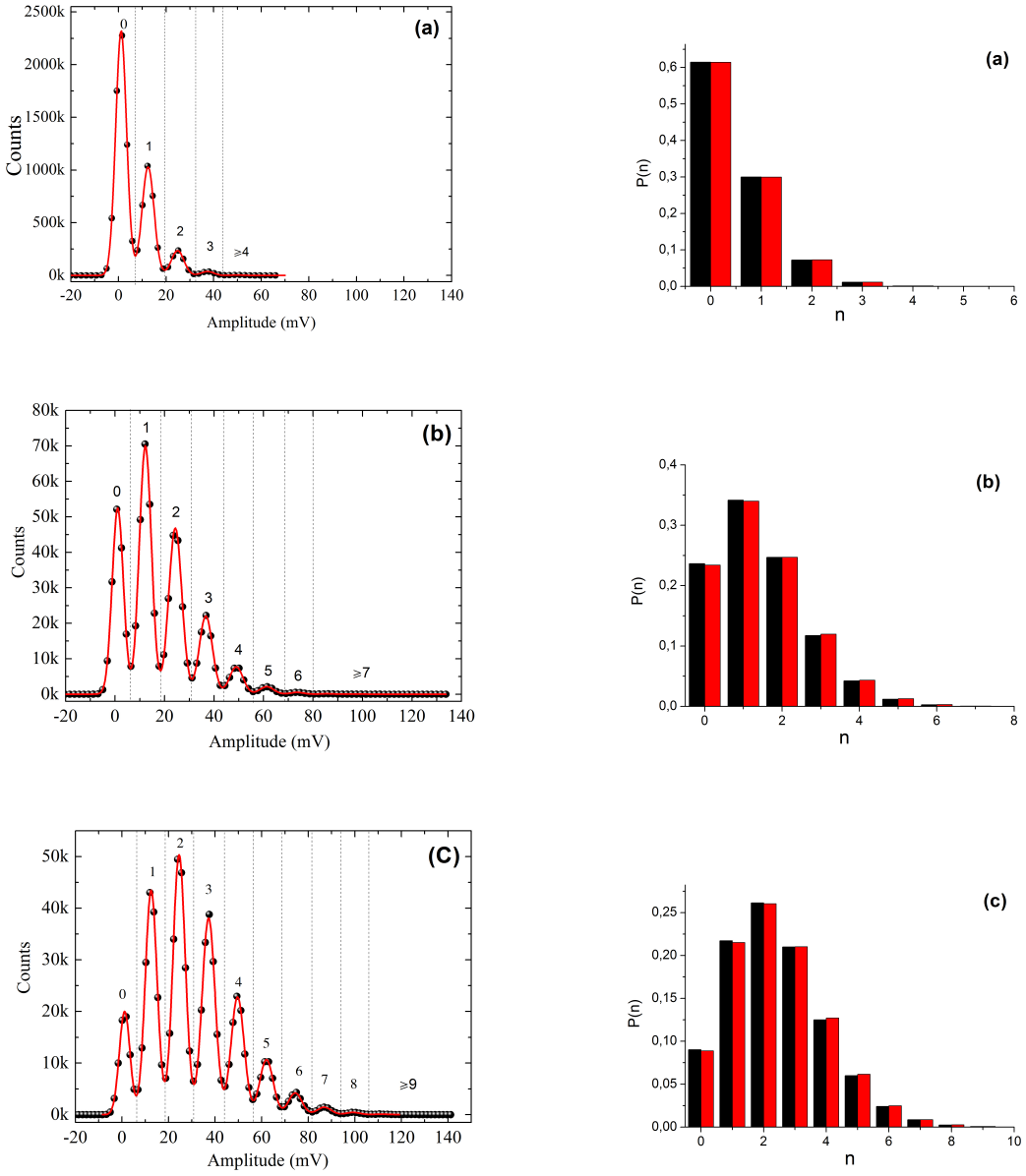

Figure 4.3: In the graphs on the left, dots represent TES counts for three different values of $|\alpha_j\rangle$, after a binning on the oscilloscope channels. Solid lines are the Gaussian fits on the experimental data, while the dotted vertical lines are the thresholds. In the graphs on the right, the experimental probability distribution (black bars) obtained for measurements binned according to the threshold is compared with the corresponding Poisson distribution of mean value $\eta\mu$ (with $\eta = 6,70\%$) (red bars). Graphs (a), (b) and (c) are obtained with a coherent state characterized by a mean photon number per pulse $\mu = 7$, $\mu = 22$ and $\mu = 36$ respectively. As evident from the plots, the experimental results are in remarkable agreement with the theoretical predictions, showing a fidelity higher than $99,99\%$ in the three cases.

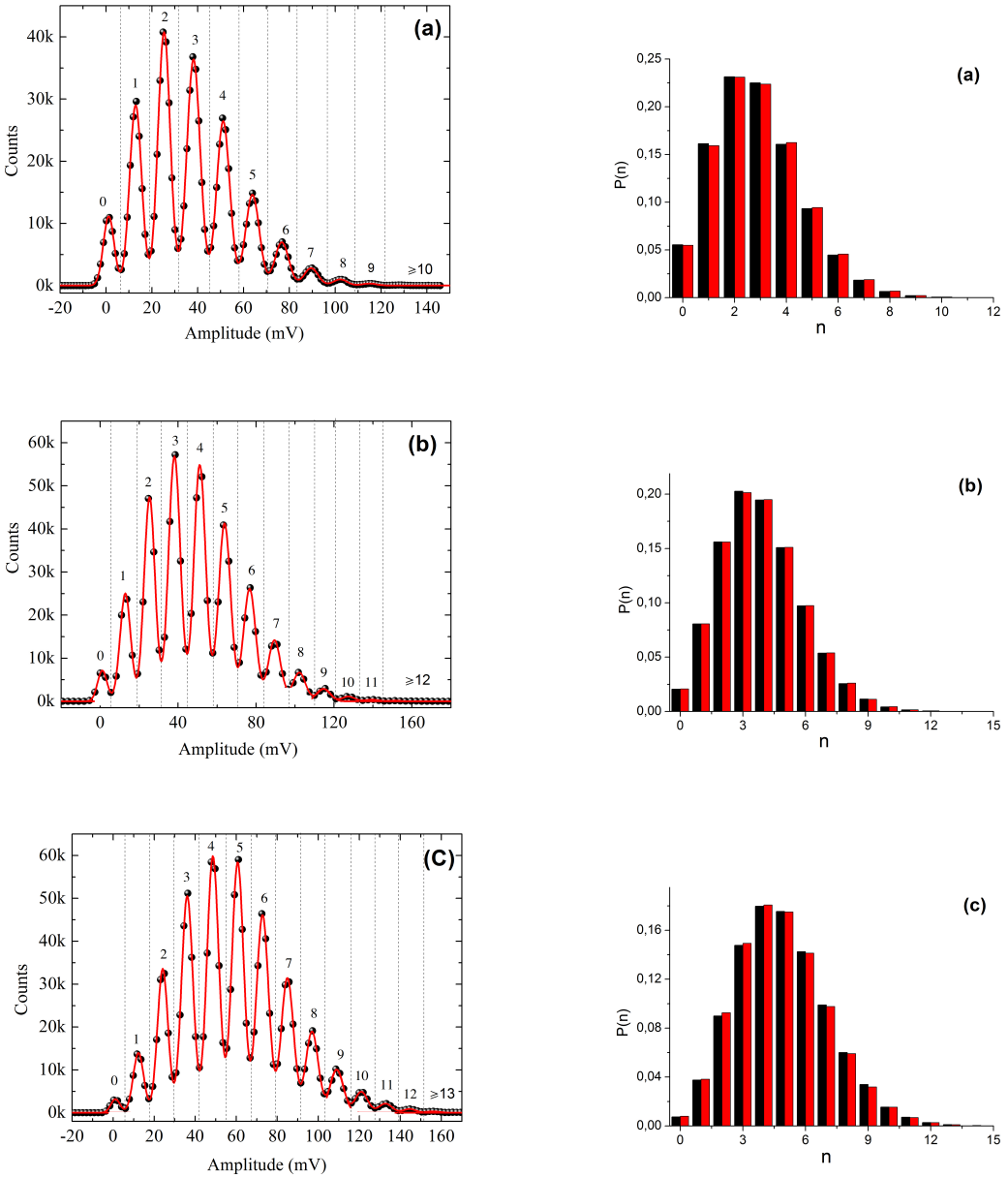

Figure 4.4: In the graphs on the left, dots represent TES counts for three different values of $|\alpha_j\rangle$. Solid lines are the Gaussian fits on the experimental data, while the dotted vertical lines are the thresholds. In the graphs of the right, the experimental probability distribution (black bars) obtained for measurements binned according to the threshold is compared with the corresponding Poisson distribution of mean value $\eta\mu$ (with $\eta = 6,70\%$) (red bars). Graphs (a), (b) and (c) are obtained with a coherent state characterized by a mean photon number per pulse $\mu = 43$, $\mu = 58$ and $\mu = 72$ respectively. The experimental results are in remarkable agreement with the theoretical predictions, showing a fidelity higher of $99,99\%$ in cases (a) and (b) and a fidelity of $99,97\%$ in case (c).